Available online at www.sciencedirect.com
SCIENCE DIRECT®
Comput. Methods Appl. Mech. Engrg. 194 (2005) 5109–5138
Computer methods in applied mechanics and engineering
www.elsevier.com/locate/cma

Implicit numerical integration of a three-invariant, isotropic/kinematic hardening cap plasticity model for geomaterials

C.D. Foster [a], R.A. Regueiro [b,*], A.F. Fossum [c], R.I. Borja [a]

[a] *Department of Civil and Environmental Engineering, Stanford University, Stanford, CA 94305, USA*
[b] *Materials and Engineering Sciences Center, Sandia National Laboratories, P.O. Box 969, MS 9405, Livermore, CA 94551-0969, USA*
[c] *Geosciences and Environment Center, Sandia National Laboratories, Albuquerque, NM 87185, USA*

Abstract

The mechanical constitutive behavior of geomaterials is quite complex, involving pressure-sensitive yielding, differences in strength in triaxial extension vs. compression, the Bauschinger effect, dependence on porosity, and other factors. Capturing these behaviors necessitates the use of fairly complicated and expensive non-linear material models. For elastically isotropic materials, such models usually involve three-invariant plasticity formulations. Spectral decomposition has been used to increase the efficiency of numerical simulation for such models for the isotropically hardening case. We modify the spectral decomposition technique to models that include kinematic hardening. Finally, we perform some numerical simulations to demonstrate quadratic convergence.

Keywords: Kinematic hardening; Spectral decomposition; Plasticity; Geomechanics; Implicit integration

1. Introduction

The mechanical behavior of rocks and concrete can involve one or several interacting micromechanical processes. In low-porosity rocks, typically the macroscopic behavior is elastic, followed by dilatancy and shear localization with loss of strength. The dilatant behavior is associated with the onset of microcrack growth [1,2]. Porous rocks exhibit more varied behavior. At low mean stresses, they often exhibit compaction, followed by significant pre-failure dilation before shear failure. The dilation can be a result

* Corresponding author. Tel.: +1 925 294 4745; fax: +1 925 294 3410.
E-mail address: raregue@sandia.gov (R.A. Regueiro).

0045-7825/$ - see front matter
doi:10.1016/j.cma.2005.01.001

of microcrack growth as above, but also grain rotation and sliding. At higher mean stresses, the material undergoes inelastic compaction resulting from pore collapse, accompanied by strain hardening. On continued loading, the material may still fail in shear.

To capture these behaviors, we will need fairly advanced constitutive models. Such models can be computationally expensive to numerically integrate. Since yield surfaces and evolution equations are not simple, the evaluations of these functions can be computationally intensive. The ability to minimize the number of function evaluations can save significant run-time costs.

Many of these materials, though certainly not all, are elastically isotropic or approximately so. This restriction can be useful in reducing computation time. For models that also have an isotropic yield function and are isotropically hardening, spectral decomposition can reduce the number of function evaluations and the number of equations to be solved. Tamagnini et al. [3] and Borja et al. [4] have recently used this approach for three-invariant models for geomaterials. The algorithm is not new, however. Simo [5–7] used spectral directions to enable a return-mapping algorithm for finite deformation plasticity.

The spectral decomposition involves the determination of the eigenvalues and eigenvectors of the stress tensor, which we will refer to as the principal values and principal directions of the tensor. Hence, the stress tensor can be written as

$$\boldsymbol{\sigma} = \sum_{A=1}^{3} \sigma_A \boldsymbol{m}^{(A)}, \tag{1}$$

where σ_A are the eigenvalues of the stress tensor,

$$\boldsymbol{m}^{(A)} = \boldsymbol{n}^{(A)} \otimes \boldsymbol{n}^{(A)} \quad \text{(no sum)} \tag{2}$$

and $\boldsymbol{n}^{(A)}$ are the corresponding eigenvectors.

For isotropic hardening and elasticity, the elastic strain, plastic strain rate, and stress tensors are coaxial, i.e. they share the same principal directions. Hence the spectral decomposition of the elastic strain tensor can be taken as an alternative to the spectral decomposition of the stress tensor.

This decomposition can be put to use in two ways. First, for isotropically hardening models, the trial stress $\boldsymbol{\sigma}^{\mathrm{tr}}_{n+1}$ and converged stress $\boldsymbol{\sigma}_{n+1}$ at time t_{n+1} have the same principal directions. If we decompose the trial stress, we automatically know the principal directions of the converged stress. Then there are only three unknowns, the principal values, needed to determine the full stress state. This number is half the six unknowns needed to determine the stress tensor using traditional algorithms. Since typically we are dealing with relatively complicated constitutive models with non-linear hardening, these can be solved for using a Newton–Raphson iteration. By reducing the number of equations by three, this algorithm is made more efficient.

Second, the spectral directions can be used to generate the consistent tangent with great efficiency. This formulation relies on the coaxiality of the stress and plastic strain increment, however, a property that is lost when we introduce kinematic hardening.

This paper presents an algorithm for the implicit numerical integration of models that have kinematic hardening or combined isotropic and kinematic hardening using the spectral decomposition of the relative stress (difference between the stress and a back stress; cf. Eq. (29)). Traditionally, these models have been integrated implicitly without spectral decomposition [8–17], a potentially more computationally costly alternative to the algorithm presented in this paper.

1.1. Notation

The summation convention, or Einstein's notation, will be used throughout the paper where not explicitly stated otherwise by the note `(no sum)`. For example, $\sigma_{ii} = \sigma_{11} + \sigma_{22} + \sigma_{33}$. In the previous section,

Eq. (1) could be written without the summation symbol and still have the same meaning. Eq. (2) does not have an implied sum only because it is explicitly indicated. Vector and tensor quantities will be written in symbolic form using boldface. Scalar quantities will not be boldface. Vector and tensor products are defined as follows: (1) The symbol '·' implies the contraction over the inner index of two vectors or tensors. For example, for vectors $\boldsymbol{a}$ and $\boldsymbol{b}$, $\boldsymbol{a}\cdot\boldsymbol{b} = a_i b_i$, and for tensors $\boldsymbol{\alpha}$ and $\boldsymbol{\beta}$, $(\boldsymbol{\alpha}\cdot\boldsymbol{\beta})_{ij} = \alpha_{ik}\beta_{kj}$. (2) Similarly, the symbol ':' represents the contraction of the innermost two indices of two tensor quantities. For example, $\boldsymbol{\alpha}:\boldsymbol{\beta} = \alpha_{ij}\beta_{ij}$ or $(\boldsymbol{C}:\boldsymbol{\epsilon})_{ij} = C_{ijkl}\epsilon_{kl}$. (3) The symbol '$\otimes$' denotes an outer or tensor product, with no contraction on any of the indices, such that $(\boldsymbol{a}\otimes\boldsymbol{b})_{ij} = a_i b_j$ and $(\boldsymbol{\alpha}\otimes\boldsymbol{\beta})_{ijkl} = \alpha_{ij}\beta_{kl}$.

2. Infinitesimal elastoplasticity

The geomaterial model is formulated within the framework of infinitesimal elastoplasticity and hence is only valid when the displacements and rotations are small. Under these conditions, the strain can be approximated by the infinitesimal strain tensor $\boldsymbol{\epsilon}$

$$\boldsymbol{\epsilon} = \boldsymbol{\nabla}^{\mathrm{s}}\boldsymbol{u} = \tfrac{1}{2}(\boldsymbol{\nabla}\boldsymbol{u} + (\boldsymbol{\nabla}\boldsymbol{u})^{\mathrm{t}}), \tag{3}$$

where $\boldsymbol{u}$ is the displacement vector, $(\bullet)^{\mathrm{t}}$ is the transpose operator, and $(\bullet)^{\mathrm{s}}$ denotes the symmetric part of the tensor. We also assume an additive decomposition of the strain tensor into elastic and plastic parts

$$\boldsymbol{\epsilon} = \boldsymbol{\epsilon}^{\mathrm{e}} + \boldsymbol{\epsilon}^{\mathrm{p}}. \tag{4}$$

Assuming that a Helmholtz free energy density function $\psi(\boldsymbol{\epsilon}^{\mathrm{e}}, \boldsymbol{\zeta})$ for isothermal conditions depends on the elastic strain $\boldsymbol{\epsilon}^{\mathrm{e}}$ and the vector of strain-like internal state variables $\boldsymbol{\zeta}$ (which will evolve with plastic flow), and following the standard thermodynamic arguments of Coleman and Noll [18,19], the Clausius–Duhem inequality (dissipation density $\mathscr{D}$) then reads

$$\mathscr{D} := \boldsymbol{\sigma} : \dot{\boldsymbol{\epsilon}}^{\mathrm{p}} - \boldsymbol{q}\cdot\dot{\boldsymbol{\zeta}} \geqslant 0, \tag{5}$$

where the stress $\boldsymbol{\sigma}$ and vector of stress-like internal state variables $\boldsymbol{q}$ are determined by

$$\boldsymbol{\sigma} = \rho\frac{\partial\psi}{\partial\boldsymbol{\epsilon}^{\mathrm{e}}}; \qquad \boldsymbol{q} := \rho\frac{\partial\psi}{\partial\boldsymbol{\zeta}}, \tag{6}$$

where ρ is the mass density. The variables $\boldsymbol{\sigma}$ and ϵ^{e}, and $\boldsymbol{q}$ and $\boldsymbol{\zeta}$, are thermodynamically conjugate.

Assuming linear elasticity and linear dependence of $\boldsymbol{q}$ on $\boldsymbol{\zeta}$, the isothermal free energy function is written in quadratic form as

$$\rho\psi(\boldsymbol{\epsilon}^{\mathrm{e}}, \boldsymbol{\zeta}) = \tfrac{1}{2}\boldsymbol{\epsilon}^{\mathrm{e}} : \boldsymbol{c}^{\mathrm{e}} : \boldsymbol{\epsilon}^{\mathrm{e}} + \tfrac{1}{2}\boldsymbol{\zeta}\cdot\boldsymbol{M}\cdot\boldsymbol{\zeta} \tag{7}$$

and the resulting constitutive equations in rate form are

$$\dot{\boldsymbol{\sigma}} = \boldsymbol{c}^{\mathrm{e}} : \dot{\boldsymbol{\epsilon}}^{\mathrm{e}} = \boldsymbol{c}^{\mathrm{e}} : (\dot{\boldsymbol{\epsilon}} - \dot{\boldsymbol{\epsilon}}^{\mathrm{p}}); \quad \dot{\boldsymbol{q}} = \boldsymbol{M}\cdot\dot{\boldsymbol{\zeta}}, \tag{8}$$

where $\boldsymbol{c}^{\mathrm{e}}$ is a constant fourth-order elasticity tensor and $\boldsymbol{M}$ a constant hardening tensor.

Based on the assumptions of the mathematical theory of plasticity, the behavior is elastic at a given stress state if a given convex yield function, $f(\boldsymbol{\sigma}, \boldsymbol{q})$, is less than zero. Plastic flow can only occur when $f = 0$, and values of $\boldsymbol{\sigma}$ and $\boldsymbol{q}$ that result in $f > 0$ are inadmissible. For a given set of internal state variables, we refer to $\{\boldsymbol{\sigma} : f(\boldsymbol{\sigma}, \boldsymbol{q}) = 0\}$ as the *yield surface*.

We assume also the existence of a plastic potential function g that dictates the direction of plastic flow via the equation

$$\dot{\boldsymbol{\epsilon}}^{\mathrm{p}} = \dot{\gamma}\frac{\partial g}{\partial\boldsymbol{\sigma}}, \tag{9}$$

where $\dot{\gamma}$ is the consistency parameter. If $g = f$, the model is associative in its plasticity. We assume also that the evolution of the internal state variables is related to $\dot{\gamma}$ via a set of hardening functions

$$\dot{\boldsymbol{\zeta}} := \dot{\gamma}\boldsymbol{h}(\boldsymbol{\sigma}, \boldsymbol{q}) \Rightarrow \dot{\boldsymbol{q}} = \dot{\gamma}\boldsymbol{M} \cdot \boldsymbol{h}(\boldsymbol{\sigma}, \boldsymbol{q}) = \dot{\gamma}\boldsymbol{h}^{q}(\boldsymbol{\sigma}, \boldsymbol{q}). \tag{10}$$

Using Eq. (10) and the consistency condition

$$0 = \dot{f} = \frac{\partial f}{\partial \boldsymbol{\sigma}} : \dot{\boldsymbol{\sigma}} + \frac{\partial f}{\partial \boldsymbol{q}} \cdot \dot{\boldsymbol{q}}, \tag{11}$$

we can solve for the consistency parameter

$$\dot{\gamma} = \frac{(\partial f/\partial \boldsymbol{\sigma}) : \boldsymbol{c}^{e} : \dot{\boldsymbol{\epsilon}}}{(\partial f/\partial \boldsymbol{\sigma}) : \boldsymbol{c}^{e} : (\partial g/\partial \boldsymbol{\sigma}) - (\partial f/\partial \boldsymbol{q}) \cdot \boldsymbol{h}^{q}} = \frac{1}{\chi}\frac{\partial f}{\partial \boldsymbol{\sigma}} : \boldsymbol{c}^{e} : \dot{\boldsymbol{\epsilon}}. \tag{12}$$

We substitute (12) into (9) and $(8)_1$ to solve for the continuum tangent modulus as

$$\dot{\boldsymbol{\sigma}} = \left(\boldsymbol{c}^{e} - \frac{1}{\chi}\boldsymbol{c}^{e} : \frac{\partial g}{\partial \boldsymbol{\sigma}} \otimes \frac{\partial f}{\partial \boldsymbol{\sigma}} : \boldsymbol{c}^{e}\right) : \dot{\boldsymbol{\epsilon}} = \boldsymbol{c}^{ep} : \dot{\boldsymbol{\epsilon}}. \tag{13}$$

3. Stress invariants

Since the model is isotropic in its elasticity, the yield function can be expressed in terms of invariants. Using invariants guarantees that the material will behave in the same manner regardless of loading direction. For a 3-by-3 symmetric matrix, there are three independent invariants. The ones we will use are:

$$I_1 = \mathrm{tr}(\boldsymbol{\sigma}), \tag{14}$$

$$J_2 = \frac{1}{2}\left(\boldsymbol{\sigma} - \frac{I_1}{3}\mathbf{1}\right) : \left(\boldsymbol{\sigma} - \frac{I_1}{3}\mathbf{1}\right) = \frac{1}{2}\boldsymbol{s} : \boldsymbol{s}, \tag{15}$$

$$J_3 = \det(\boldsymbol{s}), \tag{16}$$

where $\mathrm{tr}(\boldsymbol{\sigma}) = \sigma_{ii}$. Notice that I_1 is simply three times the mean stress. J_2 can be thought of as a generalized measure of the shear stress acting on all planes, and J_3 reflects the behavioral feature in triaxial extension and triaxial compression. This last point will be discussed in more detail in Section 4.2.

4. Geomaterial model

Moduli, yield and plastic potential functions, and hardening functions are defined in this section to specify a geomaterial constitutive model. Limited physical motivation is presented since this paper focuses on implicit numerical integration of the model. The reader is referred to [2,20] for further motivation of the model.

4.1. Constitutive equations

We assume the elastic response is isotropic, such that $\boldsymbol{c}^{e}$ has the form

$$\boldsymbol{c}^{e} = \lambda \mathbf{1} \otimes \mathbf{1} + 2\mu \boldsymbol{I}, \tag{17}$$

where $\mathbf{1}$ is the second order identity tensor, $(\mathbf{1})_{ij} = \delta_{ij}$, $\boldsymbol{I}$ is the fourth-order symmetric identity tensor, $(\boldsymbol{I})_{ijkl} = \frac{1}{2}(\delta_{ik}\delta_{jl} + \delta_{il}\delta_{jk})$, λ and μ are the Lamé constants, and δ_{ij} is the Kronecker delta.

For the internal state variables we define

$$\boldsymbol{q} := \begin{Bmatrix} \boldsymbol{\alpha} \\ \kappa \end{Bmatrix}; \qquad \boldsymbol{M} := \begin{bmatrix} c^{\alpha}\boldsymbol{I} & \boldsymbol{0} \\ \boldsymbol{0} & c^{\kappa} \end{bmatrix}, \tag{18}$$

where $\boldsymbol{\alpha}$ is the back stress associated with deviatoric plasticity and cyclic loading, κ the isotropic stress-like internal state variable associated with compaction hardening, and c^{α} and c^{κ} are hardening parameters for $\boldsymbol{\alpha}$ and κ, respectively.

4.2. Yield function

The yield surface for the model has several components to capture the various behaviors described in the introduction. At its core is an exponential shear failure function

$$F_{\mathrm{f}}(I_1) = A - C\exp(BI_1) - \theta I_1, \tag{19}$$

where A, B, C, and θ are all non-negative material parameters that are fit to the failure data, more exactly to experimental peak stress for various confining pressures. This function captures the pressure-dependence of the shear strength of these materials. The shear strength increases with more compressive mean stresses (Fig. 1), without the linear dependence associated with a simpler Mohr–Coulomb or Drucker–Prager approximation. These latter two models tend to overpredict shear strength at high pressures. The parameter θ is the asymptotic slope of this surface, recognizing that the pressure may still have some effect, though lesser, at highly compressive mean stresses. The initial yield surface is offset from the failure surface by a material parameter N, hence the first approximation of the yield function can be written as

$$f_1 = \sqrt{J_2} - (F_{\mathrm{f}} - N) \tag{20}$$

or

$$\tilde{f}_1 = J_2 - (F_{\mathrm{f}} - N)^2. \tag{21}$$

These two functions are negative, zero, and positive in the same regions. For implementation purposes, the second form will be easier and more efficient. The next step is to multiply the second term in Eq. (21) by an elliptical cap function to account for yielding in compression.

$$f_2 = J_2 - F_{\mathrm{c}}(F_{\mathrm{f}} - N)^2, \tag{22}$$

where

$$F_{\mathrm{c}}(I_1) = 1 - H(\kappa - I_1)\left(\frac{I_1 - \kappa}{X - \kappa}\right)^2, \tag{23}$$

$$X(\kappa) = \kappa - RF_{\mathrm{f}}(\kappa) \tag{24}$$

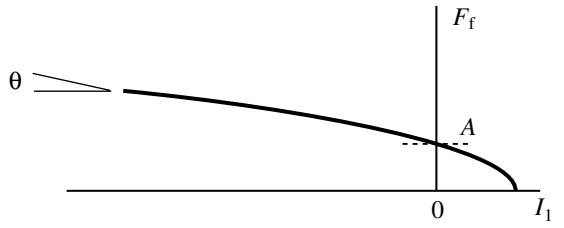

Fig. 1. Shear failure surface F_{f}.

and $H(x)$ is the Heaviside function. The effect of this function is that at some value of the mean stress, κ, the yield surface f_2 begins to deviate from the shear yield surface, and as the mean stress decreases (becomes more compressive/negative) the shear strength decreases, until a point X is reached, where there is no shear strength (Fig. 2). Hence, a smooth cap is created for the yield surface (Fig. 3). X is calculated such that the distance between κ and X is proportional to $F_f(\kappa)$, with the constant of proportionality being the material parameter R. κ is an internal state variable and will be allowed to harden. X is also an internal state variable, but is completely dependent on κ, which is the variable we will track.

Geomaterials also have a noticeably weaker strength in triaxial extension compared to triaxial compression. That is, at a given mean stress, the material will fail sooner if the principal stress that is farthest from the mean stress is so in a tensile direction rather than a compressive direction. To capture this effect, we use the Lode angle

$$\beta = \frac{-1}{3}\sin^{-1}\left(\frac{3\sqrt{3}J_3}{2(J_2)^{3/2}}\right). \tag{25}$$

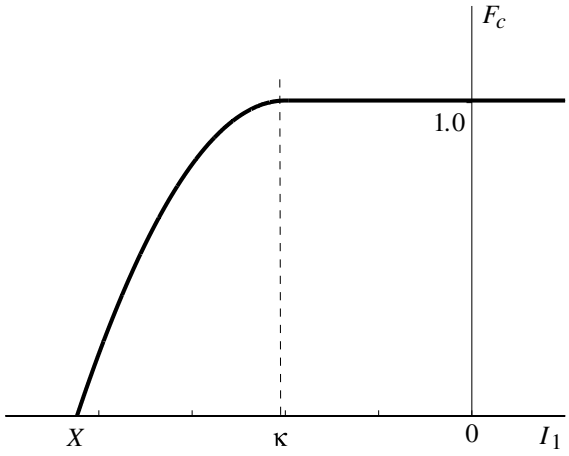

Fig. 2. Cap function F_c.

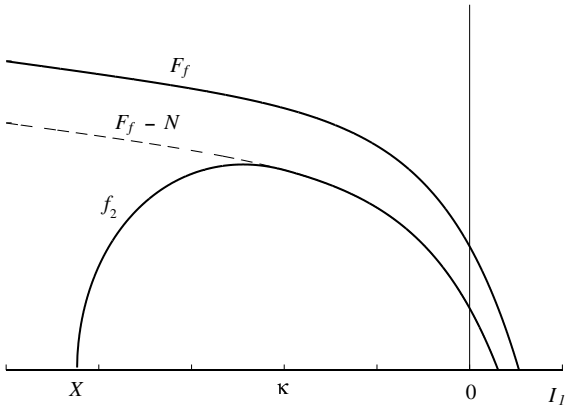

Fig. 3. Yield surface f_2 in meridional stress space, along with the shear failure surface F_f and the shear yield surface $F_f - N$.

We can now introduce the third-invariant modifying function Γ to account for this difference.

$$\Gamma(\beta) = \frac{1}{2}\left(1 + \sin 3\beta + \frac{1}{\psi}(1 - \sin 3\beta)\right) \tag{26}$$

$$= \frac{1}{2}\left(1 - \frac{3\sqrt{3}J_3}{2(J_2)^{3/2}} + \frac{1}{\psi}\left(1 + \frac{3\sqrt{3}J_3}{2(J_2)^{3/2}}\right)\right), \tag{27}$$

where ψ is the ratio of triaxial extension strength to compression strength, a material constant. Now

$$f_3 = \Gamma^2 J_2 - F_c(F_f - N)^2. \tag{28}$$

This creates a smooth Mohr–Coulomb approximation in the π-plane (Fig. 4).

The final modification to the yield surface is the introduction of the back stress tensor $\boldsymbol{\alpha}$ to capture the Bauschinger effect for cyclic loading. We use a deviatoric, translational back stress. From this we can define the relative stress

$$\boldsymbol{\xi} = \boldsymbol{\sigma} - \boldsymbol{\alpha}. \tag{29}$$

All the invariants will now be calculated from the relative stress, and we arrive at the final form of our yield function

$$f = (\Gamma^{\xi})^2 J_2^{\xi} - F_c(F_f - N)^2 = 0, \tag{30}$$

where the superscript ξ indicates that all quantities are computed from the relative stress tensor, rather than the absolute stress tensor. The back stress tensor will be deviatoric, hence quantities such as I_1, F_c, and F_f will remain unchanged.

Similarly, we introduce a plastic potential function g of the same form, but perhaps with distinct material parameters, as

$$g = (\Gamma^{\xi})^2 J_2^{\xi} - F_c^g(F_f^g - N)^2, \tag{31}$$

where

$$F_f^g(I_1) = A - C\exp(LI_1) - \phi I_1 \tag{32}$$

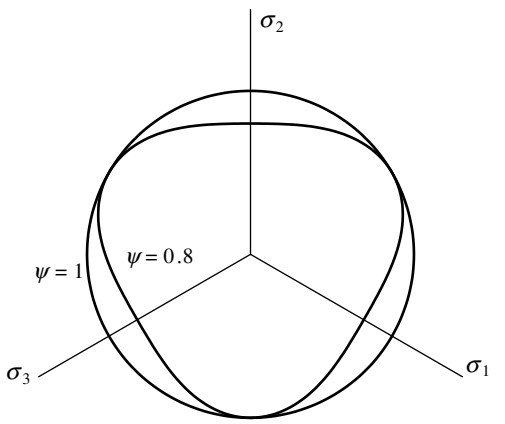

Fig. 4. Yield surface in π-plane, for $\psi = 1$ and $\psi = 0.8$.

and

$$F_{\mathrm{c}}^{g}(I_1) = 1 - H(\kappa - I_1)\left(\frac{I_1 - \kappa}{X^g - \kappa}\right)^2, \tag{33}$$

$$X^g(\kappa) = \kappa - QF_{\mathrm{f}}^{g}(\kappa), \tag{34}$$

where if $L = B$, $\phi = \theta$, and $Q = R$, plastic flow is associative. Non-associative plastic flow has been observed for low-porosity rocks [21]. The frictional strength parameters B, θ, and R typically overestimate the observed volumetric plastic deformation, warranting a non-associative model with L, ϕ, and Q determined from experimental measurements of volumetric plastic deformation.

4.3. Hardening functions

The cap hardening parameter κ and deviatoric back stress $\boldsymbol{\alpha}$ evolve with plastic deformation. As one might expect, the evolution of κ is related to mean stress, and more directly to the plastic volumetric strain, ϵ_v^{p}, while the evolution of the back stress is related to the deviatoric plastic strain, $\boldsymbol{e}^{\mathrm{p}}$.

The evolution of the back stress takes the form [2,20]

$$\dot{\boldsymbol{\alpha}} := c^{\alpha} G^{\alpha} \dot{\boldsymbol{e}}^{\mathrm{p}} = c^{\alpha} G^{\alpha}\left(\dot{\boldsymbol{\epsilon}}^{\mathrm{p}} - \frac{1}{3}\mathrm{tr}(\dot{\boldsymbol{\epsilon}}^{\mathrm{p}})\mathbf{1}\right) = c^{\alpha} G^{\alpha}\dot{\gamma}\left(\frac{\partial g}{\partial \boldsymbol{\sigma}} - \frac{1}{3}\frac{\partial g}{\partial I_1}\mathbf{1}\right), \tag{35}$$

where c^{α} is a material parameter that controls the rate of hardening, and is the same as that found in Eq. (18). G^{α} is a function which limits the growth of the back stress tensor as it approaches the failure surface. It takes the form

$$G^{\alpha}(\boldsymbol{\alpha}) = 1 - \frac{\sqrt{J_2^{\alpha}}}{N}, \qquad J_2^{\alpha} = \frac{1}{2}\boldsymbol{\alpha} : \boldsymbol{\alpha}. \tag{36}$$

As the yield surface meets the failure surface in stress space, $G^{\alpha}(\boldsymbol{\alpha}) = 0$, and further deviatoric loading leads to perfect plasticity.

To determine how the cap parameter evolves in Eq. (10), the following form for the plastic volumetric strain is used [2]:

$$\epsilon_v^{\mathrm{p}} = W(\exp\{[D_1 - D_2(X(\kappa) - X_0)](X(\kappa) - X_0)\} - 1), \tag{37}$$

if $\dot{X} < 0$ (i.e., cap hardening). X is not allowed to increase, as this would result in softening of the cap, which appears to be unphysical behavior for these materials [22,23]. $\dot{\kappa}$ has the same sign as $\dot{X}$, and hence the same restriction applies. For the case where κ is decreasing (cap hardening), we can calculate the change by noting

$$\dot{\epsilon}_v^{\mathrm{p}} = \mathrm{tr}(\dot{\boldsymbol{\epsilon}}^{\mathrm{p}}) = 3\dot{\gamma}\frac{\partial g}{\partial I_1} \tag{38}$$

and

$$\dot{\epsilon}_v^{\mathrm{p}} = \frac{\partial \epsilon_v^{\mathrm{p}}}{\partial X}\frac{\partial X}{\partial \kappa}\dot{\kappa}. \tag{39}$$

Equating Eqs. (38) and (39), the evolution equation for κ that results is

$$\dot{\kappa} = 3\dot{\gamma}\frac{\partial g}{\partial I_1}\Big/\left(\frac{\partial \epsilon_v^{\mathrm{p}}}{\partial X}\frac{\partial X}{\partial \kappa}\right). \tag{40}$$

The evolution of the strain-like internal state variables can easily be back-figured from the equations above. We define the hardening functions $\boldsymbol{h}$ for these variables as

$$\dot{\boldsymbol{\zeta}} = \dot{\gamma}\boldsymbol{h}(\boldsymbol{\sigma},\boldsymbol{q}); \quad \boldsymbol{h}(\boldsymbol{\sigma},\boldsymbol{q}) := \left\{ \begin{array}{l} G^{\alpha}(\boldsymbol{\alpha})(\partial g/\partial\boldsymbol{\sigma} - (1/3)(\partial g/\partial I_1)\mathbf{1}) \\ 3(\partial g/\partial I_1)/\left[K(\partial\epsilon_v^{\mathrm{p}}/\partial X)(\partial X/\partial\kappa)\right] \end{array} \right\}, \tag{41}$$

$$\boldsymbol{h}^{q} = \left\{ \begin{array}{l} \boldsymbol{h}^{\alpha} \\ h^{\kappa} \end{array} \right\} = \boldsymbol{M}\cdot\boldsymbol{h}(\boldsymbol{\sigma},\boldsymbol{q}), \tag{42}$$

where $K = \lambda + 2\mu/3$ is the bulk modulus, and $c^{\kappa} = K$ in Eq. (18). We could have chosen any quantity with units of stress for c^{κ}, but the bulk modulus seems natural given κ's relationship to volumetric strain.

The above equations describe the model used in this paper. However, it should be noted that a localized deformation model is being formulated that would handle post-localization response. Furthermore, the model has been extended to include the effects of non-linear elasticity, rate dependence, and transverse isotropy [20].

5. Return mapping algorithm for implicit integration

We consider a strain-driven problem. Given a strain increment $\Delta\boldsymbol{\epsilon}$ and the values of the stress and internal state variables at time t_n, the goal is to solve for the values of these variables at time t_{n+1}, using the evolution equations in (8), (9) and (41). However, simultaneous integration of these evolution equations is complicated. The typical solution to this problem is to use an approximate numerical technique. Because of its simplicity and unconditional stability, we integrate our equations using an implicit Euler scheme. While this scheme has the above mentioned advantages, we should note that it has two drawbacks: it is only first-order accurate in the time increment, and it is an implicit scheme. Using the implicit Euler approximation, the discrete versions of (8), (9), and (41) become

$$\Delta\boldsymbol{\sigma} = \boldsymbol{c}^{\mathrm{e}} : \left(\Delta\boldsymbol{\epsilon} - \Delta\gamma\left(\frac{\partial g}{\partial\boldsymbol{\sigma}}\right)_{n+1}\right), \tag{43}$$

$$\Delta\boldsymbol{\alpha} = c^{\alpha}G^{\alpha}(\boldsymbol{\alpha}_{n+1})\Delta\gamma\left(\frac{\partial g}{\partial\boldsymbol{\sigma}} - \frac{1}{3}\frac{\partial g}{\partial I_1}\mathbf{1}\right)_{n+1}, \tag{44}$$

$$\Delta\kappa = 3\Delta\gamma\left(\frac{\partial g}{\partial I_1}\Big/\left(\frac{\partial\epsilon_v^{\mathrm{p}}}{\partial X}\frac{\partial X}{\partial\kappa}\right)\right)_{n+1}, \tag{45}$$

where $\Delta\boldsymbol{\sigma} = \boldsymbol{\sigma}_{n+1} - \boldsymbol{\sigma}_n$, etc. Hence the solution of $\boldsymbol{\sigma}_{n+1}$, $\boldsymbol{\alpha}_{n+1}$, and κ_{n+1} are trivial from the above equations. Eq. (43) is often conveniently rewritten as

$$\boldsymbol{\sigma}_{n+1} = \boldsymbol{\sigma}^{\mathrm{tr}}_{n+1} - \Delta\gamma\boldsymbol{c}^{\mathrm{e}} : \left(\frac{\partial g}{\partial\boldsymbol{\sigma}}\right)_{n+1}, \tag{46}$$

where $\boldsymbol{\sigma}^{\mathrm{tr}}_{n+1}$ is the trial predictor stress based on the assumption that the increment is elastic

$$\boldsymbol{\sigma}^{\mathrm{tr}}_{n+1} = \boldsymbol{\sigma}_n + \boldsymbol{c}^{\mathrm{e}} : \Delta\boldsymbol{\epsilon}. \tag{47}$$

It is convenient to rewrite this equation further as

$$\boldsymbol{\sigma}^{\mathrm{corr}} := \boldsymbol{\sigma}_{n+1} - \boldsymbol{\sigma}^{\mathrm{tr}}_{n+1} = -\Delta\gamma\boldsymbol{c}^{\mathrm{e}} : \left(\frac{\partial g}{\partial\boldsymbol{\sigma}}\right)_{n+1}, \tag{48}$$

where $\boldsymbol{\sigma}^{\mathrm{corr}}$ is the plastic corrector for the stress increment.

In the plastic regime, the solution of these equations involves the introduction of an additional variable, the incremental consistency parameter $\Delta\gamma$. Hence we need an additional equation to solve the system of equations, and that is the yield function evaluated at time t_{n+1}

$$f_{n+1} = 0. \tag{49}$$

To solve this system of equations, functions are evaluated at time t_{n+1}. This system is typically solved by a Newton–Raphson type iteration. Our vector of unknowns is

$$\boldsymbol{Z} = \{\, \sigma_{11} \quad \sigma_{22} \quad \sigma_{33} \quad \sigma_{23} \quad \sigma_{31} \quad \sigma_{12} \quad \alpha_{11} \quad \alpha_{22} \quad \alpha_{23} \quad \alpha_{31} \quad \alpha_{12} \quad \kappa \quad \Delta\gamma \,\}^{\mathrm{t}} \tag{50}$$

and our residual vector

$$\hat{\boldsymbol{R}}(\boldsymbol{Z}) = \left\{ \begin{array}{c} \Delta\gamma c^{\mathrm{e}}_{11kl}(\partial g/\partial\sigma_{kl}) - \sigma_{11} + \sigma^{\mathrm{tr}}_{11} \\ \Delta\gamma c^{\mathrm{e}}_{22kl}(\partial g/\partial\sigma_{kl}) - \sigma_{22} + \sigma^{\mathrm{tr}}_{22} \\ \Delta\gamma c^{\mathrm{e}}_{33kl}(\partial g/\partial\sigma_{kl}) - \sigma_{33} + \sigma^{\mathrm{tr}}_{33} \\ \Delta\gamma c^{\mathrm{e}}_{23kl}(\partial g/\partial\sigma_{kl}) - \sigma_{23} + \sigma^{\mathrm{tr}}_{23} \\ \Delta\gamma c^{\mathrm{e}}_{31kl}(\partial g/\partial\sigma_{kl}) - \sigma_{31} + \sigma^{\mathrm{tr}}_{31} \\ \Delta\gamma c^{\mathrm{e}}_{12kl}(\partial g/\partial\sigma_{kl}) - \sigma_{12} + \sigma^{\mathrm{tr}}_{12} \\ \Delta\gamma (h^{\alpha})_{11} - \alpha_{11} + (\alpha_{11})_n \\ \Delta\gamma (h^{\alpha})_{22} - \alpha_{22} + (\alpha_{22})_n \\ \Delta\gamma (h^{\alpha})_{23} - \alpha_{23} + (\alpha_{23})_n \\ \Delta\gamma (h^{\alpha})_{31} - \alpha_{31} + (\alpha_{31})_n \\ \Delta\gamma (h^{\alpha})_{12} - \alpha_{12} + (\alpha_{12})_n \\ \Delta\gamma h^{\kappa} - \kappa + \kappa_n \\ f \end{array} \right\} = \boldsymbol{0}, \tag{51}$$

where subscript $n+1$ is left off to simplify notation. Here $\alpha_{33} = -(\alpha_{11} + \alpha_{22})$ can be eliminated since the back stress is deviatoric. Even condensing out α_{33}, we are left with 13 equations and 13 unknowns. The linear system has to be solved several times as we iterate to find the solution.

We could save time in this algorithm if we could reduce the number of unknowns. Not only would this reduce the size of the matrix to be inverted, but it would also reduce the number of function evaluations, which is expensive given the complexity of the yield function and evolution equations. Tamagnini et al. [3] and Borja et al. [4] have used spectral decomposition to do this in the case of the isotropic hardening models. However, these algorithms rely on the fact that the trial stress $\boldsymbol{\sigma}^{\mathrm{tr}}_{n+1}$ has the same spectral directions as $\partial g/\partial\boldsymbol{\sigma}$ (and from this the converged stress also has the same spectral directions). This is not in general true for kinematically hardening models. In fact, recall that for the relative stress $\boldsymbol{\xi} = \boldsymbol{\sigma} - \boldsymbol{\alpha}$, we can see that

$$\frac{\partial g}{\partial \boldsymbol{\sigma}} = \frac{\partial g}{\partial \boldsymbol{\xi}} \frac{\partial \boldsymbol{\xi}}{\partial \boldsymbol{\sigma}} = \frac{\partial g}{\partial \boldsymbol{\xi}}. \tag{52}$$

Since the plastic potential function g depends only on the invariants of the relative stress, it is easy to show that $\boldsymbol{\xi}$ and $\partial g/\partial\boldsymbol{\xi}$ have the same spectral directions. Clearly, the spectral directions of the stress and relative stress may be different. The approach of spectrally decomposing the relative stress, however, has promise. From Eq. (48), $\boldsymbol{\sigma}^{\mathrm{corr}}$ also will have the same spectral directions as the relative stress since multiplication by an isotropic tensor $\boldsymbol{c}^{\mathrm{e}}$ preserves spectral directions. From Eq. (44), since $\mathbf{1}$ is hydrostatic and can have any spectral decomposition, $\Delta\boldsymbol{\alpha}$ also will have the same spectral directions as the relative stress. Finally, the trial relative stress can be written as

$$\boldsymbol{\xi}^{\mathrm{tr}}_{n+1} = \boldsymbol{\sigma}^{\mathrm{tr}}_{n+1} - \boldsymbol{\alpha}_n = \boldsymbol{\xi}_{n+1} - \boldsymbol{\sigma}^{\mathrm{corr}} + \Delta\boldsymbol{\alpha} \tag{53}$$

such that it shares the same spectral directions as the converged relative stress $\boldsymbol{\xi}_{n+1}$, plastic corrector stress $\boldsymbol{\sigma}^{\text{corr}}$, and back stress increment $\Delta\boldsymbol{\alpha}$. The trial relative stress $\boldsymbol{\xi}^{\text{tr}}_{n+1}$ is the critical quantity because it is known a priori.

We calculate the trial relative stress and spectrally decompose it using a Jacobi iteration. While this method is slow for larger matrices, speed of convergence was good for these 3-by-3 matrices. The algorithm is described in [24] among many other places. We have chosen to express the yield condition in terms of the principal relative stresses, so we use the trial relative stresses to check yielding.

If there is yielding, we would like to put the spectral decomposition to good use. As we have noted, however, the tensor unknowns for which we need to solve, the stress and back stress, do not share the same spectral decomposition. To avoid this difficulty, we modify the unknowns that we iterate. We can easily update the stress and back stress if we have $\boldsymbol{\sigma}^{\text{corr}}$ and $\Delta\boldsymbol{\alpha}$. Since we already have the spectral directions for those tensors, we only need to solve for the principal values.

Hence the vector of unknowns becomes

$$\boldsymbol{X} = \{\, \sigma^{\text{corr}}_{\text{I}} \quad \sigma^{\text{corr}}_{\text{II}} \quad \sigma^{\text{corr}}_{\text{III}} \quad \Delta\alpha_{\text{I}} \quad \Delta\alpha_{\text{II}} \quad \Delta\kappa \quad \Delta\gamma \,\}^{\text{t}}. \tag{54}$$

Again, $\Delta\alpha_{\text{III}}$ is eliminated since the back stress is deviatoric.

Using a change of coordinates to the principal directions, the residual vector then becomes

$$\boldsymbol{R} = \begin{Bmatrix} \Delta\gamma a^{\text{e}}_{1A}(\partial g/\partial\xi_A) + \sigma^{\text{corr}}_{\text{I}} \\ \Delta\gamma a^{\text{e}}_{2A}(\partial g/\partial\xi_A) + \sigma^{\text{corr}}_{\text{II}} \\ \Delta\gamma a^{\text{e}}_{3A}(\partial g/\partial\xi_A) + \sigma^{\text{corr}}_{\text{III}} \\ \Delta\gamma(h^{\alpha})_{\text{I}} - \Delta\alpha_{\text{I}} \\ \Delta\gamma(h^{\alpha})_{\text{II}} - \Delta\alpha_{\text{II}} \\ \Delta\gamma h^{\kappa} - \Delta\kappa \\ f \end{Bmatrix} = \boldsymbol{0}, \tag{55}$$

where subscript $n+1$ is left off, and the tensor $\boldsymbol{a}^{\text{e}}$ is the elasticity tensor projected to principal relative stress space,

$$\boldsymbol{a}^{\text{e}} = \begin{bmatrix} \lambda+2\mu & \lambda & \lambda \\ \lambda & \lambda+2\mu & \lambda \\ \lambda & \lambda & \lambda+2\mu \end{bmatrix}. \tag{56}$$

Since the yield and hardening functions are expressed in terms of stress invariants, the easiest way to calculate the derivatives is

$$\frac{\partial(\bullet)}{\partial\xi_A} = \frac{\partial(\bullet)}{\partial I_1}\frac{\partial I_1}{\partial\xi_A} + \frac{\partial(\bullet)}{\partial J^{\xi}_2}\frac{\partial J^{\xi}_2}{\partial\xi_A} + \frac{\partial(\bullet)}{\partial J^{\xi}_3}\frac{\partial J^{\xi}_3}{\partial\xi_A} \tag{57}$$

$$= \frac{\partial(\bullet)}{\partial I_1} + \frac{\partial(\bullet)}{\partial J^{\xi}_2}\left(\xi_A - \frac{1}{3}I_1\right) + \frac{\partial(\bullet)}{\partial J^{\xi}_3}\left[\left(\xi_A - \frac{1}{3}I_1\right)^2 - \frac{2}{3}J^{\xi}_2\right]. \tag{58}$$

The smaller system can now be solved using a Newton–Raphson iteration

$$\boldsymbol{X}^{k+1}_{n+1} = \boldsymbol{X}^{k}_{n+1} - \left[\left(\frac{\text{D}\boldsymbol{R}}{\text{D}\boldsymbol{X}}\right)^{k}_{n+1}\right]^{-1}\boldsymbol{R}^{k}_{n+1}, \tag{59}$$

where in practice the inverse is not explicitly computed, and the equations are solved using an LU decomposition; $k+1$ refers to the current iteration. Since the updates to the stress and back stress may not have the same spectral decomposition as the stress and back stress themselves, we update as follows:

$$\boldsymbol{\sigma} = \boldsymbol{\sigma}^{\mathrm{tr}} + \sum_{A=1}^{3} \sigma_A^{\mathrm{corr}} \boldsymbol{m}^{(A)}, \tag{60}$$

$$\boldsymbol{\alpha} = \boldsymbol{\alpha}_n + \sum_{B=1}^{2} \Delta\alpha_B (\boldsymbol{m}^{(B)} - \boldsymbol{m}^{(\mathrm{III})}), \tag{61}$$

$$\kappa = \kappa_n + \Delta\kappa, \tag{62}$$

where the subscript $n+1$ is left off to simplify notation. Here the index B runs only from 1 to 2, since only two independent principal values of the evolution of the back stress are calculated.

This algorithm is summarized in Box 1.

Box 1. Summary of stress-point algorithm

Step 1. Compute $\boldsymbol{\sigma}^{\mathrm{tr}}_{n+1} = \boldsymbol{\sigma}_n + \boldsymbol{c}^{\mathrm{e}} : \Delta\boldsymbol{\epsilon}$
Step 2. Spectrally decompose $\boldsymbol{\xi}^{\mathrm{tr}}_{n+1} = \boldsymbol{\sigma}^{\mathrm{tr}}_{n+1} - \boldsymbol{\alpha}_n = \sum_{A=1}^{3} \xi^{\mathrm{tr}}_A \boldsymbol{m}^{(A)}$
Step 3. Check yielding: is $f > 0$?
If no, set $\boldsymbol{\sigma}_{n+1} = \boldsymbol{\sigma}^{\mathrm{tr}}_{n+1}$ and exit.
Step 4. If yes, set $\boldsymbol{X}_0 = \boldsymbol{0}$ and iterate:
$\delta\boldsymbol{X}^k = [(-\mathrm{D}\boldsymbol{R}/\mathrm{D}\boldsymbol{X})^k]^{-1}\boldsymbol{R}(\boldsymbol{X}^k)$
$\boldsymbol{X}^{k+1} = \boldsymbol{X}^k + \delta\boldsymbol{X}^k$
until $(R_\sigma/R_{\sigma,\max}) < \mathrm{tol}_\sigma$, $(R_\alpha/R_{\alpha,\max}) < \mathrm{tol}_\alpha$, $(R_\kappa/R_{\kappa,\max}) < \mathrm{tol}_\kappa$,
$(R_{\mathrm{f}}/R_{f,\max}) < \mathrm{tol}_{\mathrm{f}}$
Step 5. Update:
$\boldsymbol{\sigma}_{n+1} = \boldsymbol{\sigma}^{\mathrm{tr}}_{n+1} + \sum_{A=1}^{3} \sigma_A^{\mathrm{corr}} \boldsymbol{m}^{(A)}$
$\boldsymbol{\alpha}_{n+1} = \boldsymbol{\alpha}_n + \sum_{B=1}^{2} \Delta\alpha_B (\boldsymbol{m}^{(B)} - \boldsymbol{m}^{(\mathrm{III})})$
$\kappa_{n+1} = \kappa_n + \Delta\kappa$
$\gamma_{n+1} = \gamma_n + \Delta\gamma$
and exit.

Remark 1. The tolerances have to be treated carefully. Because the units of the yield function, and hence the last element of the residual vector, are those of stress squared, the value of that component may differ by several orders of magnitude from the other components. Hence, convergence of the last component can mask lack of convergence by other components, or lack of convergence of the last component may be masked by convergence of the other components. Hence, we check that each component of the residual is converging. Noting that the initial value of the first six components of the residual vector is zero, we must also ensure that the maximum values of the residual components are compared to as we iterate.

Remark 2. Note that if, in addition to the yield function, the hardening functions depend only on the relative stress, the number of variables in the local Newton–Raphson iteration can be further reduced. If we examine

$$\boldsymbol{\xi}^{\text{corr}} = \boldsymbol{\xi} - \boldsymbol{\xi}^{\text{tr}} = \boldsymbol{\sigma}^{\text{corr}} - \Delta\boldsymbol{\alpha}, \tag{63}$$

then we can form a residual based on the equation

$$(\boldsymbol{\xi}^{\text{corr}})_A = \Delta\gamma\left(-a^{\text{e}}_{AB}\frac{\partial g}{\partial \xi_B} + (h^{\alpha})_A\right). \tag{64}$$

The corrections to the stress and back stress can then be calculated once the Newton–Raphson iteration has converged. Unfortunately, this strategy cannot be employed for the current model because one of the factors of $\boldsymbol{h}^{\alpha}$ is the function $G^{\alpha}(\boldsymbol{\alpha})$ defined in Eq. (36) whose evaluation requires the updated value of the back stress. Fortunately, however, this equation only affects the evolution of $\boldsymbol{\alpha}$ in a scalar fashion, and hence does not affect the spectral directions of the back stress increment.

Remark 3. There is an additional strategy that can be employed to reduce the number of equations. Notice that the last diagonal term of the matrix $\mathrm{D}\boldsymbol{R}/\mathrm{D}\boldsymbol{X}$, the term $\partial f/\partial\Delta\gamma$, is 0. This can be used to statically condense out the last variable as described in Simo and Hughes [6] and Tamagnini et al. [3].

Remark 4. The algorithm summarized in Box 1 is applicable to isotropic-kinematic hardening models for which elasticity is isotropic and for which the spectral directions of the back stress rate $\dot{\boldsymbol{\alpha}}$ in Eq. (35) are the same as those of the relative stress $\boldsymbol{\xi}$. The algorithm is not applicable to integrating models that do not share these features.

6. Consistent tangent

The consistent tangent modulus, also referred to as the algorithmic tangent modulus [6], is an essential part of the finite element formulation for the implicit model. For isotropic hardening, Tamagnini et al. [3] and Borja et al. [4] have used spectral directions to form the consistent tangent in a highly efficient, closed-form fashion. However, this formulation relies on the fact that, for isotropic hardening, the stress and plastic strain increment have the same spectral directions. This coaxiality is lost in the kinematically hardening case.

We form the consistent tangent in a traditional manner. For an implicit Euler scheme, we start with the following system of equations:

$$\boldsymbol{0} = \left\{\begin{array}{c} (\boldsymbol{c}^{\text{e}})^{-1}\boldsymbol{\sigma}_{n+1} - \boldsymbol{\epsilon}_{n+1} + \boldsymbol{\epsilon}^{\text{p}}_n + \Delta\gamma(\partial g/\partial\boldsymbol{\sigma})_{n+1} \\ \boldsymbol{q}_{n+1} - \boldsymbol{q}_n - \Delta\gamma(\boldsymbol{h}^q)_{n+1} \\ f(\boldsymbol{\sigma}_{n+1}, \boldsymbol{q}_{n+1}) \end{array}\right\}. \tag{65}$$

Differentiating the equations with respect to $\boldsymbol{\epsilon}_{n+1}$ and arranging the results, we can obtain the matrix equations

$$\begin{bmatrix} \boldsymbol{I} \\ \boldsymbol{0} \\ \boldsymbol{0} \end{bmatrix} = \underbrace{\begin{bmatrix} (\boldsymbol{c}^{\text{e}})^{-1} + \Delta\gamma\dfrac{\partial^2 g}{\partial\boldsymbol{\sigma}\partial\boldsymbol{\sigma}} & \Delta\gamma\dfrac{\partial^2 g}{\partial\boldsymbol{\sigma}\partial\boldsymbol{q}} & \partial g/\partial\boldsymbol{\sigma} \\ -\Delta\gamma(\partial\boldsymbol{h}^q/\partial\boldsymbol{\sigma}) & \boldsymbol{1} - \Delta\gamma(\partial\boldsymbol{h}^q/\partial\boldsymbol{q}) & -\boldsymbol{h}^q \\ (\partial f/\partial\boldsymbol{\sigma})^{\text{t}} & (\partial f/\partial\boldsymbol{q})^{\text{t}} & 0 \end{bmatrix}}_{\boldsymbol{A}} \begin{bmatrix} \partial\boldsymbol{\sigma}/\partial\boldsymbol{\epsilon} \\ \partial\boldsymbol{q}/\partial\boldsymbol{\epsilon} \\ (\partial\Delta\gamma/\partial\boldsymbol{\epsilon})^{\text{t}} \end{bmatrix}. \tag{66}$$

The $n+1$ subscripts have been omitted for simplicity. Clearly, then, the consistent tangent $\boldsymbol{c}_{n+1} = (\partial\boldsymbol{\sigma}/\partial\boldsymbol{\epsilon})_{n+1}$ is the upper left 6-by-6 submatrix of $\boldsymbol{A}^{-1}$.

As with the integration point algorithm, notice that the system can be statically condensed by taking advantage of the fact that the last diagonal entry is zero. Partitioning the last row and column off the matrix $\boldsymbol{A}$, the equations can be condensed in the same way as those for the local iteration. After some manipulation, the equations become

$$\begin{bmatrix} \boldsymbol{I} \\ \boldsymbol{0} \end{bmatrix} - \frac{1}{\chi} \begin{Bmatrix} \partial g/\partial \boldsymbol{\sigma} \\ -\boldsymbol{h}^q \end{Bmatrix} \left\{ \left(\frac{\partial f}{\partial \boldsymbol{\sigma}} \right)^{\mathrm{t}} \left(\frac{\partial f}{\partial \boldsymbol{q}} \right)^{\mathrm{t}} \right\} \boldsymbol{B}^{-1} \begin{bmatrix} \boldsymbol{I} \\ \boldsymbol{0} \end{bmatrix} = \boldsymbol{B} \begin{bmatrix} \partial \boldsymbol{\sigma}/\partial \boldsymbol{\epsilon} \\ \partial \boldsymbol{q}/\partial \boldsymbol{\epsilon} \end{bmatrix}, \tag{67}$$

where

$$\boldsymbol{B} = \begin{bmatrix} (\boldsymbol{c}^{\mathrm{e}})^{-1} + \Delta\gamma \dfrac{\partial^2 g}{\partial \boldsymbol{\sigma} \partial \boldsymbol{\sigma}} & \Delta\gamma \dfrac{\partial^2 g}{\partial \boldsymbol{\sigma} \partial \boldsymbol{q}} \\ -\Delta\gamma (\partial \boldsymbol{h}^q / \partial \boldsymbol{\sigma}) & \boldsymbol{1} - \Delta\gamma (\partial \boldsymbol{h}^q / \partial \boldsymbol{q}) \end{bmatrix} \tag{68}$$

and

$$\chi = \begin{Bmatrix} \partial g/\partial \boldsymbol{\sigma} \\ -\boldsymbol{h}^q \end{Bmatrix} \boldsymbol{B}^{-1} \left\{ \left(\frac{\partial f}{\partial \boldsymbol{\sigma}} \right)^{\mathrm{t}} \left(\frac{\partial f}{\partial \boldsymbol{q}} \right)^{\mathrm{t}} \right\}. \tag{69}$$

This can be rewritten as

$$\begin{bmatrix} \partial \boldsymbol{\sigma}/\partial \boldsymbol{\epsilon} \\ \partial \boldsymbol{q}/\partial \boldsymbol{\epsilon} \end{bmatrix} = \left(\boldsymbol{B}^{-1} - \frac{1}{\chi} \boldsymbol{B}^{-1} \begin{Bmatrix} \partial g/\partial \boldsymbol{\sigma} \\ -\boldsymbol{h}^q \end{Bmatrix} \otimes \boldsymbol{B}^{-t} \begin{Bmatrix} \partial f/\partial \boldsymbol{\sigma} \\ \partial f/\partial \boldsymbol{q} \end{Bmatrix} \right) \begin{bmatrix} \boldsymbol{I} \\ \boldsymbol{0} \end{bmatrix}, \tag{70}$$

which is very similar to the formulation found in [6,25].

Finally, it should be noted that the quantities that populate the matrix $\boldsymbol{A}$ can be easily obtained from quantities that have already been calculated. For example

$$\frac{\partial f}{\partial \boldsymbol{\sigma}} = \frac{\partial f}{\partial \xi_A} \frac{\partial \xi_A}{\partial \boldsymbol{\sigma}} = \frac{\partial f}{\partial \xi_A} \boldsymbol{m}^{(A)} \tag{71}$$

and

$$\frac{\partial^2 g}{\partial \boldsymbol{\sigma} \partial \boldsymbol{\sigma}} = \frac{\partial^2 g}{\partial \xi_A \partial \xi_B} \boldsymbol{m}^{(A)} \otimes \boldsymbol{m}^{(B)}. \tag{72}$$

7. Numerical examples

All the examples are run with the associative version of the model. Time step sizes are chosen as large as possible in order to demonstrate reasonably smooth stress–strain curves.

The first example is a one element test with fully constrained degrees of freedom designed to test the local return-mapping algorithm. The example consists of two loadings: uniaxial strain in compression (prescribed displacements in the axial direction and zero displacement in the other directions), followed by constrained shearing. A simple compression simulation would not have adequately tested the ability of the implementation to operate when the spectral directions are changing.

The material properties were fit to Salem limestone data [20] and are shown in Box 2.

The stress–strain response is shown in Fig. 5. During the first loading increment, the axial response begins as elastic and then becomes plastic, while the shear stress and strain remain zero. During the second phase, the shear response is plastic, and the axial stress drops. The stress paths for the compression and shear phases are shown in Figs. 6 and 7 on the $\sqrt{J_2}$ vs. I_1 and $\sqrt{J_2^{\xi}}$ vs. I_1 planes, respectively. Recall from

Box 2. Material properties for Salem limestone

Young's modulus $E = 22{,}547$ MPa
Poisson's ratio $v = 0.2524$ (dimensionless)
$A = 689.2$ MPa
$B = 3.94\text{e}{-4}$ 1/MPa
$C = 675.2$ MPa
$\theta = 0.0$ rad
$R = 28.0$ (dimensionless)
$\kappa_0 = -8.05$ MPa
$W = 0.08$ (dimensionless)
$D_1 = 1.47\text{e}{-3}$ 1/MPa
$D_2 = 0.0$ 1/MPa^2
$c^{\alpha} = 1\text{e}5$ MPa
$\psi = 1.0$ (dimensionless)
$N = 6.0$ MPa

Eq. (30) that the yield function is a function of the invariants I_1, J_2^{ξ}, and J_3^{ξ}. When plotting stress paths in the $\sqrt{J_2}$ vs. I_1 plane, we expect the stress path to appear to deviate from the yield surface, whereas in fact the stress path moves out of plane because the principal directions of $\boldsymbol{\xi}$ are changing. We plot the stress path in the $\sqrt{J_2}$ vs. I_1 plane in order to show translation of the yield surface due to evolving $\boldsymbol{\alpha}$. Plotting the stress path in the $\sqrt{J_2^{\xi}}$ vs. I_1 plane, however, we expect the stress path to remain on the yield surface, assuming $\psi = 1$ (i.e., no dependence on J_3^{ξ}), because even though the principal directions of $\boldsymbol{\xi}$ are changing, J_2^{ξ} is invariant to these changes.

A post-localization model has not been implemented here, as the strain extends to four percent. While the results are consistent with the model as implemented, they do not capture the physical behavior of the

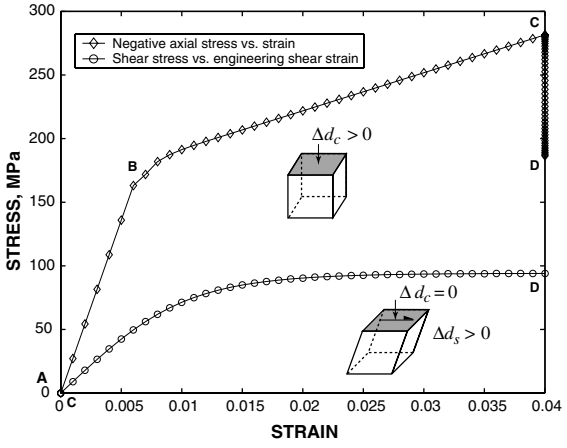

Fig. 5. Stress–strain response for uniaxial strain in compression followed by constrained shear test. Shaded face has prescribed compression displacement d_c and shear displacement d_s, while all other faces are fixed except during shear. Letters A through D indicate the loading path. Note that C and D on the compression curve appear on a vertical line since during the shear phase there is no displacement in the compression direction, i.e. $\Delta d_c = 0$, although the axial stress drops.

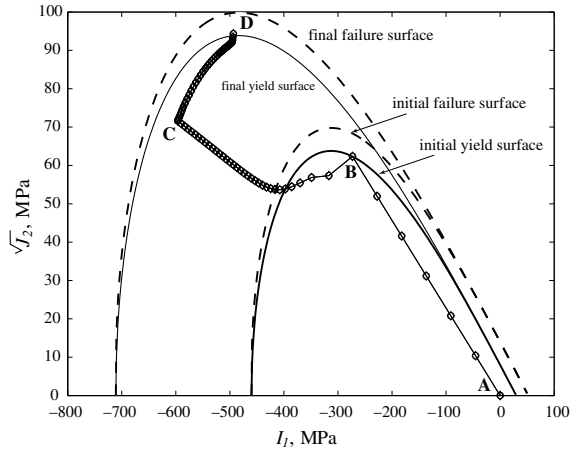

Fig. 6. Stress path in meridional stress space $\sqrt{J_2}$ vs. I_1 for compression and shear phases of uniaxial strain and constrained shear problem. Initial and final surfaces for compression and shear phases shown. The letters indicate points on the stress path that correspond with points on the stress–strain curve in Fig. 5.

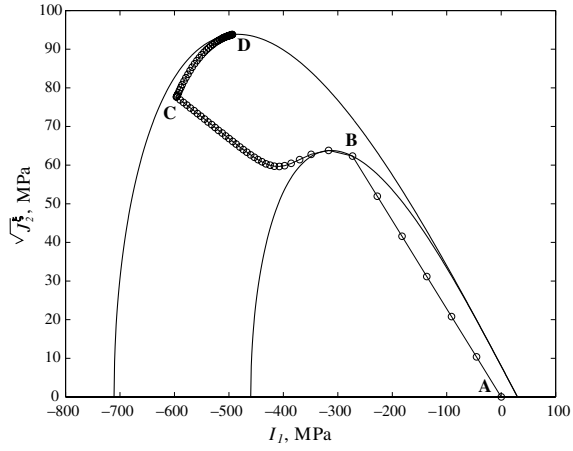

Fig. 7. Stress path in meridional stress space $\sqrt{J_2^{\xi}}$ vs. I_1 for compression and shear phases of uniaxial strain and constrained shear problem. Initial and final yield surfaces shown. The letters indicate points on the stress path that correspond with points on the stress–strain curve in Fig. 5.

material as it is deformed to larger strains. The results underscore the need to add a localization capability to this implementation of the model.

We check the convergence of the algorithm both at the first plastic step and the first step of the shear part of the test, where the spectral directions change. The resulting norm of the residual vector for both cases is plotted in Fig. 8 and also shown in Table 1. Quadratic convergence is observed. In this problem, quadratic convergence can be observed in each component of the residual vector. As discussed earlier, because of the nature of the residual vector, convergence of each component is checked. In some other problems not shown here, one larger component may hamper the quadratic convergence of other components, but overall quadratic convergence is still observed in all the examples we have run.

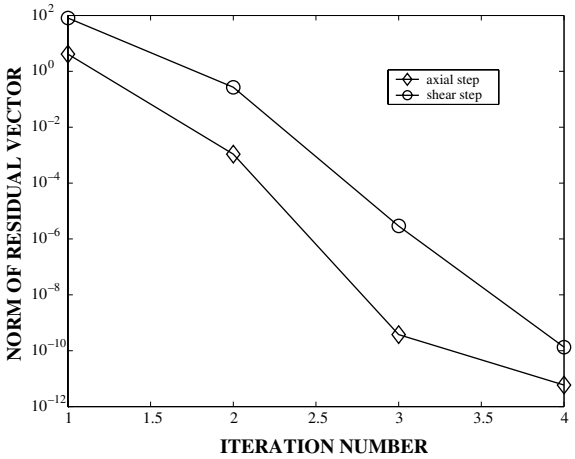

Fig. 8. Residual norm per iteration for the first plastic step in both the compressive portion and shear portion of the uniaxial strain test. Quadratic convergence is observed.

Table 1
Convergence of integration point algorithm: norm of the residual vector

Iteration number	Residual norm – compression step	Residual norm – shear step
1	4.127771E+00	8.102731E+01
2	1.088910E−03	2.699950E−01
3	3.771775E−10	2.897466E−06
4	5.911716E−12	1.346052E−10

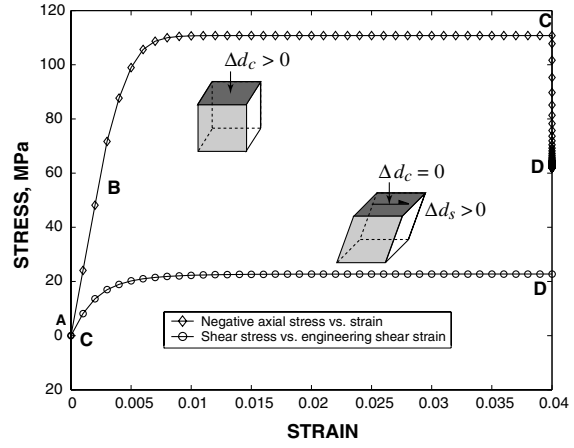

Fig. 9. Stress–strain response for element in plane stress compression and constrained shear. Compression displacement d_c and shear displacement d_s applied to darker face, while the lighter face is free. The unshaded faces have fixed normal displacements, except during shear. Letters A through D indicate points on the stress–strain curve that correspond to letters on the stress paths in Figs. 10 and 11. Note that C and D on the compression curve appear on a vertical line since during the shear phase there is no displacement in the compression direction, i.e. $\Delta d_c = 0$, although axial stress decreases.

For the second example, we verify that the consistent tangent is calculated correctly such that quadratic convergence is exhibited. To do this, we run the same problem we did to verify the stress point algorithm in the first example, but allow free movement in the orthogonal direction that does not have prescribed axial or shear displacements. Essentially, this is a plane stress version of the uniaxial strain and constrained shear problem run for the first example. This problem is run in a fully three-dimensional setting to give the prob-

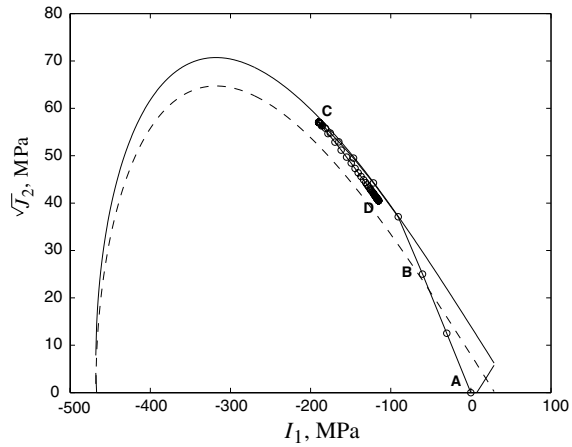

Fig. 10. Stress path in meridional stress space $\sqrt{J_2}$ vs. I_1 for compression and shear phases of plane stress problem. The letters indicate points on the stress path that correspond with points on the stress–strain curve in Fig. 9. The stress path appears to deviate from the yield surface, but it is actually moving out of plane from the $\sqrt{J_2}$ vs. I_1 plane as the principal directions of $\boldsymbol{\xi}$ change. The dashed curve shows the initial yield surface and the solid curve the translated yield surface, which at this stage is the same as the failure surface.

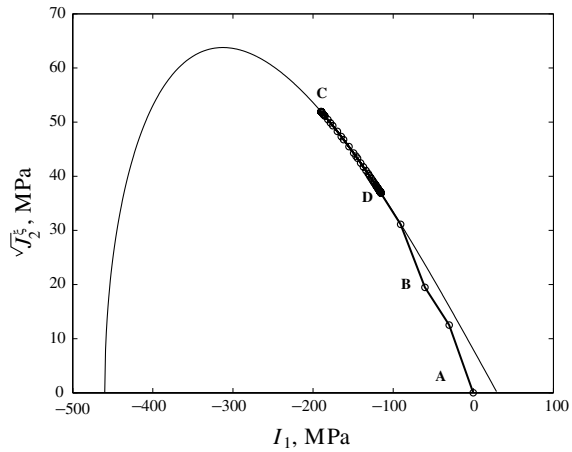

Fig. 11. Stress path in meridional stress space $\sqrt{J_2^{\xi}}$ vs. I_1 for compression and shear phases of plane stress problem. The letters indicate points on the stress path that correspond with points on the stress–strain curve in Fig. 9. The final yield surface is shown. As opposed to Fig. 10, in this figure the stress path remains on the yield surface because J_2^{ξ} and I_1 are the invariants in the yield function. The relative stress $\boldsymbol{\xi}$ is embedded in J_2^{ξ}, and so even as its principal directions change, J_2^{ξ} is invariant to these changes. The kink at point B along the stress path is due to the backstress $\boldsymbol{\alpha}$ increasing at a faster rate than the deviatoric stress $\boldsymbol{s}$ during the first plastic time step, hence resulting in an apparent softer response at point B.

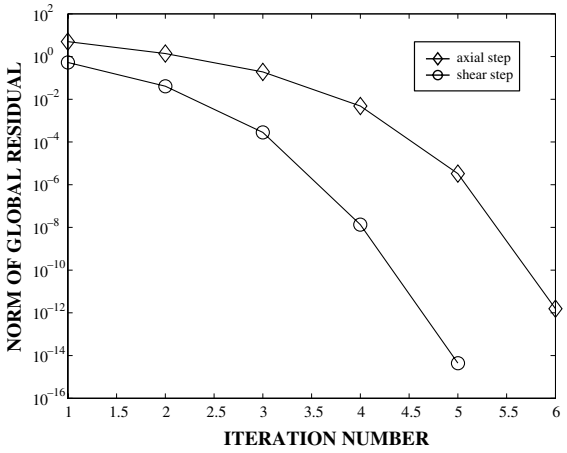

Fig. 12. Residual norm per iteration for the first plastic step in both the compression portion and shear portion of the plane stress test for the global algorithm. Quadratic convergence is observed.

Table 2
Convergence of global algorithm: norm of the global residual vector

Iteration number	Residual norm – compression step	Residual norm – shear step
1	5.0010E+00	5.2760E−01
2	1.3852E+00	4.0716E−02
3	1.9048E−01	2.7998E−04
4	4.8349E−03	1.3410E−08
5	3.2879E−06	4.4431E−15
6	1.5667E−12	

lem unconstrained degrees of freedom, as are all numerical examples in this paper. The stress–strain response is shown in Fig. 9. The stress paths for compression and shear phases are shown in Figs. 10 and 11 on the $\sqrt{J_2}$ vs. I_1 and $\sqrt{J_2^{\xi}}$ vs. I_1 planes, respectively. Again, the test has two parts, compression and shear, and we verify that the global residual vector converges quadratically (cf. Fig. 12 and Table 2).

The third example is a comparison between the implicit implementation and an existing explicit (forward Euler) implementation of the same model [2,20]. The problem is a plane strain, one-element, loading/unloading problem to 2.5% compressive strain. A 20 MPa confining pressure is applied. The explicit algorithm was run in 5000 steps to achieve stability, while the implicit needed only 80 steps to achieve a smooth stress–strain curve. As Fig. 13 shows, the results are comparable. The material properties are the same as for the first example.

Next, we continue cycling this loading, from 0% to −2.5%, to verify that the model exhibits a Bauschinger effect. The material data for this model suggests a Baushinger effect for this Limestone, which is observed in Fig. 14. The stress path is shown in Figs. 15 and 16 on the $\sqrt{J_2}$ vs. I_1 and $\sqrt{J_2^{\xi}}$ vs. I_1 planes, respectively.

Finally, to capture the difference in triaxial extension strength vs. triaxial compression strength, new material properties are required. The material properties used in the previous three examples were set for $\psi = 1$, indicating no difference in strength between triaxial extension and compression. New material properties, also fit for a limestone are given in Box 3.

Box 3. Material properties for limestone accounting for difference in triaxial extension vs. compression strength

Young's modulus $E = 22{,}547$ MPa
Poisson's ratio $v = 0.2524$ (dimensionless)
$A = 843.0$ MPa
$B = 2.73\text{e}{-4}$ 1/MPa
$C = 822.0$ MPa
$\theta = 0.0$ rad
$R = 28.0$ (dimensionless)
$\kappa_0 = -8.05$ MPa
$W = 0.08$ (dimensionless)
$D_1 = 1.47\text{e}{-3}$ 1/MPa
$D_2 = 0.0$ 1/MPa^2
$c^\alpha = 1\text{e}3$ MPa
$\psi = 0.8$ (dimensionless)
$N = 8.0$ MPa

These properties were used in two tests. Both tests were run at zero mean stress with the stress tensor

$$\boldsymbol{\sigma} = \begin{bmatrix} \sigma & 0 & 0 \\ 0 & -\sigma/2 & 0 \\ 0 & 0 & -\sigma/2 \end{bmatrix}. \tag{73}$$

For the triaxial extension test, σ is positive, while it is negative for the triaxial compression test. The results in Fig. 17 show that the material yields sooner and undergoes more plastic deformation in the triaxial extension case. Figs. 18 and 19 show how the stress paths in the π-plane meet and translate the yield surfaces for triaxial extension and compression loadings.

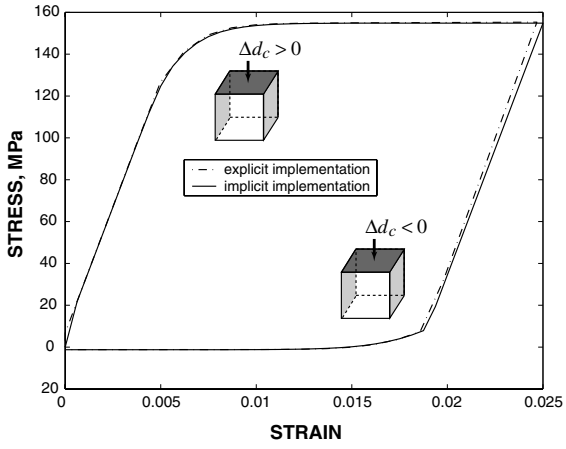

Fig. 13. Comparison between implicit (this paper) and explicit [2] implementations of the model. Plane strain compression and unloading with 20 MPa confining pressure. Compression displacement d_c applied to darker face, while confining pressure is applied to lighter faces. The unshaded faces have fixed normal displacements.

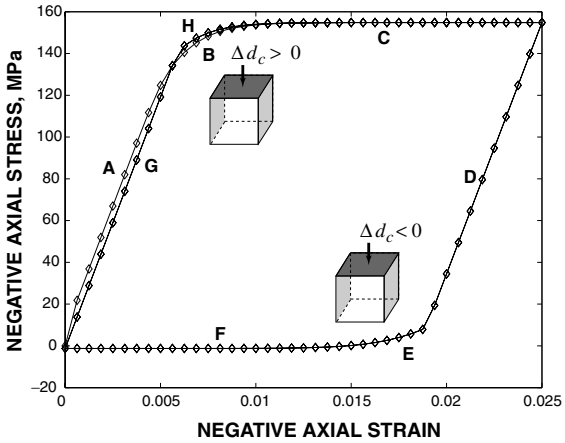

Fig. 14. The Bauschinger, or Masing, effect captured by the model. Cyclic plane strain compression with 20 MPa confining pressure. Compression displacement d_c applied to darker face, while confining pressure is applied to lighter faces. The unshaded faces have fixed normal displacements. The letters on the stress–strain curve correspond with the stress paths in Figs. 15 and 16.

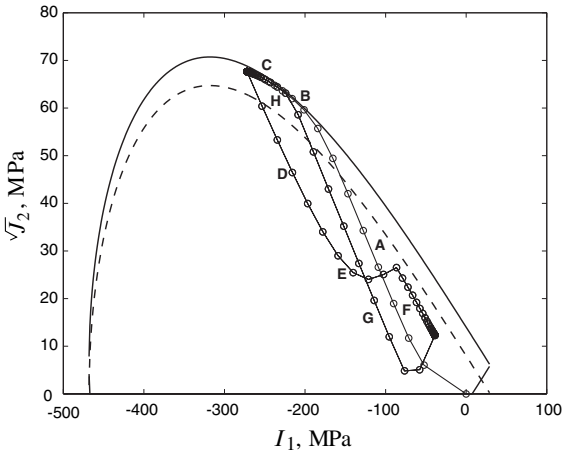

Fig. 15. Stress path in meridional stress space $\sqrt{J_2}$ vs. I_1 for compression and shear phases of plane stress problem. The letters indicate points on the stress path that correspond with points on the stress–strain curve in Fig. 14. The stress path appears to deviate from the yield surface at F along the stress path, but it is actually moving out of plane from the $\sqrt{J_2}$ vs. I_1 plane as the principal directions of ξ change. The dashed curve is the initial yield surface and the solid curve the final, translated yield surface. The initial kink in the stress path along A is due to simultaneous application of confining pressure and compression displacement d_c in the first time step.

8. Conclusions

We have reviewed a model for porous geomaterials such as limestones, sandstones, and concrete, that includes both isotropic and kinematic hardening. We have presented an algorithm for the implicit integration of models that have kinematic hardening or combined isotropic and kinematic hardening using the spectral decomposition of the relative stress. The local return mapping algorithm is an extension of algorithms used for isotropically hardening models as shown in [5,4,3]. The spectral decomposition technique

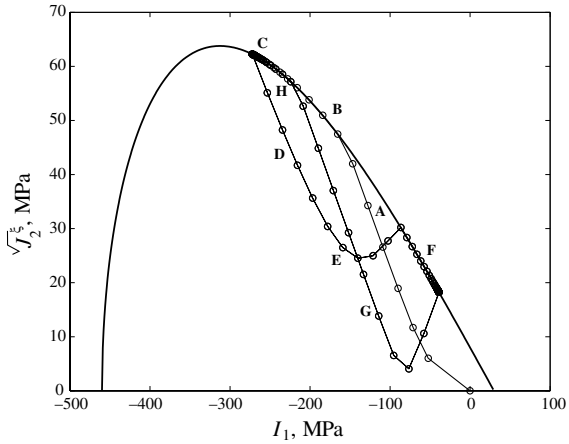

Fig. 16. Stress path in meridional stress space $\sqrt{J_2^\xi}$ vs. I_1 for compression and shear phases of plane stress problem. The letters indicate points on the stress path that correspond with points on the stress–strain curve in Fig. 14. As opposed to Fig. 15, in this figure the stress path remains on the yield surface because J_2^ξ and I_1 are invariants in the yield function, and J_2^ξ is invariant to changing principal directions of $\boldsymbol{\xi}$.

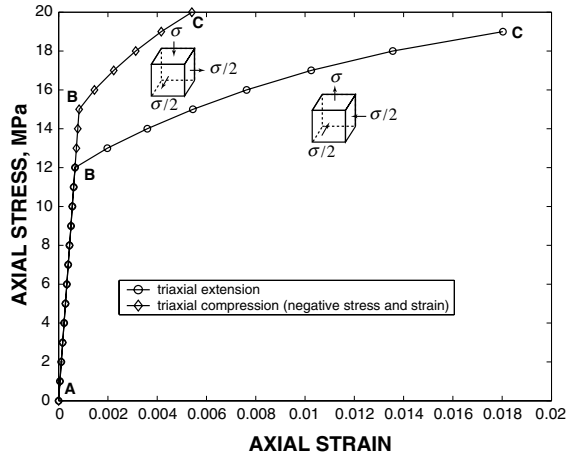

Fig. 17. Comparison of material response in trixial extension vs. triaxial compression at zero mean stress. Axial stresses are the principal stresses largest in magnitude. The letters denote points on the stress–strain curves that correspond to points on the stress paths in Figs. 18 and 19.

reduces the number of function evaluations, which can be quite costly for even moderately advanced constitutive models, as well as reduces the size of the system of equations to be solved.

The consistent tangent has been implemented in a standard way [7,25], noting that the quantities needed to form the generalized compliance can be computed from the spectral values without any additional function evaluations. However, the efficient methods used to compute the consistent tangent in the isotropically hardening case [26,4,3] cannot be used for the kinematically hardening case since the stress and strain are not coaxial.

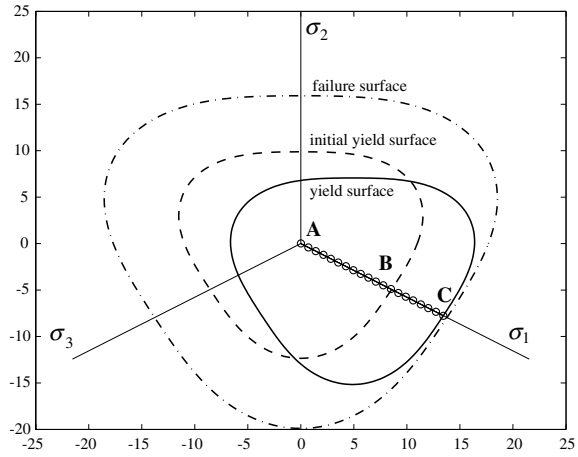

Fig. 18. Stress path in π-plane for triaxial extension showing intersection with initial yield surface and stopping at final yield surface. The failure surface is shown for reference. The letters denote points on the stress path that correspond with points on the stress–strain curve in Fig. 17.

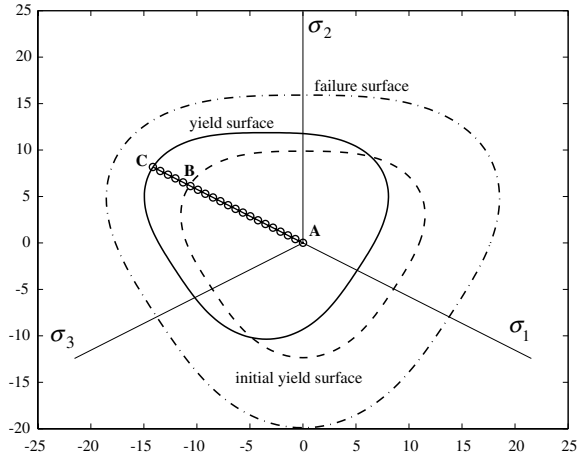

Fig. 19. Stress path in π-plane for triaxial compression showing intersection with initial yield surface and stopping at final yield surface. The failure surface is shown for reference. The letters denote points on the stress path that correspond with points on the stress–strain curve in Fig. 17.

Numerical examples show that both the local and global iterations exhibit quadratic convergence. Also, these examples show how the model can be used to capture some of the behaviors common to geomaterials, including strain hardening, the Bauschinger effect, and differences in triaxial extension vs. compression strength.

Acknowledgments

We would like to acknowledge Patrick Klein for his generous assistance with the model implementation in a research finite element code.

The first author acknowledges support from both the Swanson Foundation Achievement Rewards for College Scientists Stanford Graduate Fellowship and the Engineering Summer Sciences Institute Program at Sandia National Laboratories, California.

The first and fourth authors acknowledge the support of United States Department of Energy grant number DE-FG02-03ER15454 to Stanford University.

The second and third authors acknowledge Sandia's Laboratory Directed Research and Development program.

Sandia is a multiprogram laboratory operated by Sandia Corporation, a Lockheed Martin Company, for the United States Department of Energy under contract DE-ACO4-94AL85000.

Appendix A. Derivatives for plastic potential

There are several ways to calculate the stress gradients of the plastic potential function. Particularly convenient to potentials expressed in terms of invariants is the following:

$$\frac{\partial g}{\partial \boldsymbol{\sigma}} = \frac{\partial g}{\partial I_1}\frac{\partial I_1}{\partial \boldsymbol{\sigma}} + \frac{\partial g}{\partial J_2^{\xi}}\frac{\partial J_2^{\xi}}{\partial \boldsymbol{\sigma}} + \frac{\partial g}{\partial J_3^{\xi}}\frac{\partial J_3^{\xi}}{\partial \boldsymbol{\sigma}}, \tag{A.1}$$

where

$$\frac{\partial I_1}{\partial \boldsymbol{\sigma}} = \mathbf{1}, \tag{A.2}$$

$$\frac{\partial J_2^{\xi}}{\partial \boldsymbol{\sigma}} = \boldsymbol{\xi} - \frac{I_1}{3}\mathbf{1} = \mathrm{dev}(\boldsymbol{\xi}) = \boldsymbol{s}^{\xi}, \tag{A.3}$$

$$\frac{\partial J_3^{\xi}}{\partial \boldsymbol{\sigma}} = \left(\boldsymbol{s}^{\xi}\cdot\boldsymbol{s}^{\xi} - \frac{2}{3}J_2^{\xi}\mathbf{1}\right). \tag{A.4}$$

It may also be convenient to note the last two of the above tensors are purely deviatoric. Hence

$$\mathrm{dev}\frac{\partial g}{\partial \boldsymbol{\sigma}} = \frac{\partial g}{\partial J_2^{\xi}}\frac{\partial J_2^{\xi}}{\partial \boldsymbol{\sigma}} + \frac{\partial g}{\partial J_3^{\xi}}\frac{\partial J_3^{\xi}}{\partial \boldsymbol{\sigma}}. \tag{A.5}$$

Similarly, the spectral values of the gradients can be calculated as

$$\frac{\partial g}{\partial \sigma_A} = \frac{\partial g}{\partial I_1}\frac{\partial I_1}{\partial \sigma_A} + \frac{\partial g}{\partial J_2^{\xi}}\frac{\partial J_2^{\xi}}{\partial \sigma_A} + \frac{\partial g}{\partial J_3^{\xi}}\frac{\partial J_3^{\xi}}{\partial \sigma_A} \tag{A.6}$$

for $A = 1$, 2, or 3, where

$$\frac{\partial I_1}{\partial \sigma_A} = 1, \tag{A.7}$$

$$\frac{\partial J_2^{\xi}}{\partial \sigma_A} = \xi_A - \frac{I_1}{3} = (\mathrm{dev}(\boldsymbol{\xi}))_A = s_A^{\xi}, \tag{A.8}$$

$$\frac{\partial J_3^{\xi}}{\partial \sigma_A} = (s^{\xi})^2 - \frac{2}{3}J_2^{\xi}. \tag{A.9}$$

All that is left is to calculate the derivatives of the potential function with respect to the invariants. For our potential:

$$\frac{\partial g}{\partial I_1} = -(F_{\mathrm{f}}^g - N)\left[2F_{\mathrm{c}}^g \frac{\partial F_{\mathrm{f}}^g}{\partial I_1} + (F_{\mathrm{f}}^g - N)\frac{\partial F_{\mathrm{c}}^g}{\partial I_1}\right], \tag{A.10}$$

$$\frac{\partial F_{\mathrm{f}}^g}{\partial I_1} = -(LC\exp(LI_1) + \phi), \tag{A.11}$$

$$\frac{\partial F_{\mathrm{c}}^g}{\partial I_1} = H(\kappa - I_1)\frac{-2(I_1 - \kappa)}{(X^g(\kappa) - \kappa)^2}, \tag{A.12}$$

$$\frac{\partial g}{\partial J_2^\xi} = 2\Gamma\frac{\partial \Gamma}{\partial J_2^\xi}J_2^\xi + \Gamma^2 = \frac{\partial f}{\partial J_2^\xi}, \tag{A.13}$$

$$\frac{\partial \Gamma}{\partial J_2^\xi} = \frac{9\sqrt{3}J_3^\xi}{8(J_2^\xi)^{5/2}}\left(1 - \frac{1}{\psi}\right), \tag{A.14}$$

$$\frac{\partial g}{\partial J_3^\xi} = 2\Gamma\frac{\partial \Gamma}{\partial J_3^\xi}J_2^\xi = \frac{\partial f}{\partial J_3^\xi}, \tag{A.15}$$

$$\frac{\partial \Gamma}{\partial J_3^\xi} = \frac{-3\sqrt{3}}{4(J_2^\xi)^{3/2}}\left(1 - \frac{1}{\psi}\right). \tag{A.16}$$

The derivatives of the yield function are completely analogous.

Appendix B. Derivatives for integration point algorithm

The derivatives used in computing the derivative of the residual vector for the local integration point algorithm are as follows:

$$\begin{aligned}\frac{\partial R_1}{\partial \sigma_A^{\mathrm{corr}}} &= \delta_{1A} + \Delta\gamma a_{1B}^{\mathrm{e}}\frac{\partial}{\partial \sigma_A^{\mathrm{corr}}}\left[\frac{\partial g}{\partial \boldsymbol{\sigma}}\right]_B \\ &= \delta_{1A} + \Delta\gamma a_{1B}^{\mathrm{e}}\frac{\partial^2 g}{\partial \xi_A \partial \xi_B} \quad \text{for } A = 1,2,3,\end{aligned} \tag{B.1}$$

$$\begin{aligned}\frac{\partial^2 g}{\partial \xi_A \partial \xi_B} &= \frac{\partial}{\partial \xi_B}\left[\frac{\partial g}{\partial I_1} + \frac{\partial g}{\partial J_2^\xi}s_A^\xi + \frac{\partial g}{\partial J_3^\xi}\left((s_A^\xi)^2 - \frac{2}{3}J_2^\xi\right)\right] \\ &= \frac{\partial^2 g}{\partial I_1^2} + \frac{\partial g}{\partial J_2^\xi}\left(\delta_{AB} - \frac{1}{3}\right) + \frac{\partial^2 g}{(\partial J_2^\xi)^2}s_A^\xi s_B^\xi + \frac{\partial^2 g}{\partial J_2^\xi \partial J_3^\xi}s_A^\xi s_B^\xi \\ &\quad + \frac{\partial g}{\partial J_3^\xi}\left[2s_A^\xi \delta_{AB} - \frac{2}{3}\left(s_A^\xi + s_B^\xi\right)\right] \\ &\quad + \left(\frac{\partial^2 g}{\partial J_2^\xi \partial J_3^\xi} + \frac{\partial^2 g}{(\partial J_2^\xi)^2}\right)\left((s_A^\xi)^2 - \frac{2}{3}J_2^\xi\right) \quad \text{(no sum)},\end{aligned} \tag{B.2}$$

$$\frac{\partial^2 g}{\partial I_1^2} = -\left(2F_{\mathrm{c}}^g\left(\frac{\partial F_{\mathrm{f}}^g}{\partial I_1}\right)^2 + 4(F_{\mathrm{f}}^g - N)\frac{\partial F_{\mathrm{c}}^g}{\partial I_1}\frac{\partial F_{\mathrm{f}}^g}{\partial I_1} + 2(F_{\mathrm{f}}^g - N)F_{\mathrm{c}}^g\frac{\partial^2 F_{\mathrm{f}}^g}{\partial I_1^2} + (F_{\mathrm{f}}^g - N)^2\frac{\partial^2 F_{\mathrm{c}}^g}{\partial I_1^2}\right), \tag{B.3}$$

$$\frac{\partial^2 g}{\partial (J_2^\xi)^2} = 2J_2^\xi\left(\left(\frac{\partial \Gamma}{\partial J_2^\xi}\right)^2 + \Gamma\frac{\partial^2 \Gamma}{\partial (J_2^\xi)^2}\right) + 4\Gamma\frac{\partial \Gamma}{\partial J_2^\xi}, \tag{B.4}$$

$$\frac{\partial^2 g}{\partial (J_3^\xi)^2} = 2\left(\frac{\partial \Gamma}{\partial J_3^\xi}\right)^2 J_2^\xi, \tag{B.5}$$

$$\frac{\partial R_2}{\partial \sigma_A^{\mathrm{corr}}} = \delta_{2A} + \Delta\gamma a_{2B}^{\mathrm{e}}\frac{\partial^2 g}{\partial \xi_A \partial \xi_B}, \tag{B.6}$$

$$\frac{\partial R_3}{\partial \sigma_A^{\mathrm{corr}}} = \delta_{3A} + \Delta\gamma a_{3B}^{\mathrm{e}}\frac{\partial^2 g}{\partial \xi_A \partial \xi_B} \tag{B.7}$$

and

$$\frac{\partial R_1}{\partial \Delta\alpha_A} = \Delta\gamma a_{1B}^{\mathrm{e}}\frac{\partial}{\partial \Delta\alpha_A}\left(\frac{\partial g}{\partial \xi_B}\right) \quad \text{for } A = 1, 2, \tag{B.8}$$

$$\frac{\partial}{\partial \Delta\alpha_A}\left(\frac{\partial g}{\partial \xi_B}\right) = \frac{\partial^2 g}{\partial \xi_3 \partial \xi_B} - \frac{\partial^2 g}{\partial \xi_A \partial \xi_B}, \tag{B.9}$$

$$\frac{\partial R_2}{\partial \Delta\alpha_A} = \Delta\gamma a_{2B}^{\mathrm{e}}\frac{\partial}{\partial \Delta\alpha_A}\left(\frac{\partial g}{\partial \xi_B}\right), \tag{B.10}$$

$$\frac{\partial R_3}{\partial \Delta\alpha_A} = \Delta\gamma a_{3B}^{\mathrm{e}}\frac{\partial}{\partial \Delta\alpha_A}\left(\frac{\partial g}{\partial \xi_B}\right) \tag{B.11}$$

and

$$\frac{\partial R_1}{\partial \Delta\kappa} = \Delta\gamma a_{1B}^{\mathrm{e}}\frac{\partial}{\partial \Delta\kappa}\left(\frac{\partial g}{\partial \xi_B}\right), \tag{B.12}$$

$$\frac{\partial}{\partial \Delta\kappa}\left(\frac{\partial g}{\partial \xi_B}\right) = \frac{\partial^2 g}{\partial \kappa \partial I_1}, \tag{B.13}$$

$$\frac{\partial^2 g}{\partial \kappa \partial I_1} = -(F_{\mathrm{f}}^g - N)\left(2\frac{\partial F_{\mathrm{c}}^g}{\partial \kappa}\frac{\partial F_{\mathrm{f}}^g}{\partial I_1} + (F_{\mathrm{f}}^g - N)\frac{\partial^2 F_{\mathrm{c}}^g}{\partial \kappa \partial I_1}\right), \tag{B.14}$$

$$\frac{\partial R_2}{\partial \Delta\kappa} = \Delta\gamma a_{2B}^{\mathrm{e}}\frac{\partial}{\partial \Delta\kappa}\left(\frac{\partial g}{\partial \xi_B}\right), \tag{B.15}$$

$$\frac{\partial R_3}{\partial \Delta\kappa} = \Delta\gamma a_{3B}^{\mathrm{e}}\frac{\partial}{\partial \Delta\kappa}\left(\frac{\partial g}{\partial \xi_B}\right) \tag{B.16}$$

and

$$\frac{\partial R_1}{\partial \Delta\gamma} = a^{\mathrm{e}}_{1B}\left(\frac{\partial g}{\partial \xi_B}\right), \tag{B.17}$$

$$\frac{\partial R_2}{\partial \Delta\gamma} = a^{\mathrm{e}}_{2B}\left(\frac{\partial g}{\partial \xi_B}\right), \tag{B.18}$$

$$\frac{\partial R_3}{\partial \Delta\gamma} = a^{\mathrm{e}}_{3B}\left(\frac{\partial g}{\partial \xi_B}\right), \tag{B.19}$$

$$\frac{\partial R_4}{\partial \sigma^{\mathrm{corr}}_A} = \Delta\gamma \frac{\partial h^{\alpha}_1}{\partial \sigma^{\mathrm{corr}}_A}, \tag{B.20}$$

$$\begin{aligned}\frac{\partial h^{\alpha}_B}{\partial \sigma^{\mathrm{corr}}_A} &= c^{\alpha} G^{\alpha} \frac{\partial}{\partial \sigma^{\mathrm{corr}}_A}\left(\frac{\partial g}{\partial \xi_B} - \frac{\partial g}{\partial I_1}\right) \\ &= c^{\alpha} G^{\alpha}\left(\frac{\partial^2 g}{\partial \xi_A \partial \xi_B} - \frac{\partial^2 g}{\partial I_1^2}\right) \quad \text{for } A = 1,2,3 \text{ and } B = 1,2,\end{aligned} \tag{B.21}$$

$$\frac{\partial R_5}{\partial \sigma^{\mathrm{corr}}_A} = \Delta\gamma \frac{\partial h^{\alpha}_2}{\partial \sigma^{\mathrm{corr}}_A} \tag{B.22}$$

and

$$\frac{\partial R_4}{\partial \Delta\alpha_A} = \Delta\gamma \frac{\partial h^{\alpha}_1}{\partial \Delta\alpha_A} - \delta_{1A} \tag{B.23}$$

$$\frac{\partial h^{\alpha}_B}{\partial \Delta\alpha_A} = c^{\alpha} \frac{\partial G^{\alpha}}{\partial \Delta\alpha_A}\left(\frac{\partial g}{\partial \xi_B} - \frac{\partial g}{\partial I_1}\right) + c^{\alpha} G^{\alpha}\left(\frac{\partial^2 g}{\partial \xi_3 \partial \xi_B} - \frac{\partial^2 g}{\partial \xi_A \partial \xi_B}\right), \tag{B.24}$$

$$\frac{\partial R_5}{\partial \Delta\alpha_A} = \Delta\gamma \frac{\partial h^{\alpha}_2}{\partial \Delta\alpha_A} - \delta_{2A} \tag{B.25}$$

and

$$\frac{\partial R_4}{\partial \Delta\kappa} = 0, \tag{B.26}$$

$$\frac{\partial R_5}{\partial \Delta\kappa} = 0, \tag{B.27}$$

$$\frac{\partial R_4}{\partial \Delta\gamma} = h^{\alpha}_1, \tag{B.28}$$

$$\frac{\partial R_5}{\partial \Delta\gamma} = h^{\alpha}_2 \tag{B.29}$$

and

$$\frac{\partial R_6}{\partial \sigma^{\mathrm{corr}}_A} = \Delta\gamma \frac{\partial h^{\kappa}}{\partial \sigma^{\mathrm{corr}}_A} = \frac{3\Delta\gamma}{(\partial X^g/\partial\kappa)(\partial \epsilon^{\mathrm{p}}_v/\partial X^g)} \frac{\partial}{\partial \sigma^{\mathrm{corr}}_A}\left(\frac{\partial g}{\partial I_1}\right) = \frac{3\Delta\gamma}{(\partial X^g/\partial\kappa)(\partial \epsilon^{\mathrm{p}}_v/\partial X^g)} \frac{\partial^2 g}{\partial I_1^2}, \tag{B.30}$$

$$\frac{\partial R_6}{\partial \Delta\alpha_A} = 0, \tag{B.31}$$

$$\frac{\partial R_6}{\partial \Delta\kappa} = \Delta\gamma \frac{\partial h^\kappa}{\partial \kappa} - 1, \tag{B.32}$$

$$\frac{\partial R_6}{\partial \Delta\gamma} = h^\kappa \tag{B.33}$$

and

$$\frac{\partial R_7}{\partial \sigma_A^{\mathrm{corr}}} = \frac{\partial f}{\partial \xi_A}, \tag{B.34}$$

$$\frac{\partial R_7}{\partial \Delta\alpha_A} = \frac{\partial f}{\partial \Delta\alpha_A} = \frac{\partial f}{\partial \xi_3} - \frac{\partial f}{\partial \xi_A}, \tag{B.35}$$

$$\frac{\partial R_7}{\partial \Delta\kappa} = \frac{\partial f}{\partial \kappa} = -(F_{\mathrm{f}} - N)^2 \frac{\partial F_{\mathrm{c}}}{\partial \kappa}. \tag{B.36}$$

Appendix C. Derivatives for consistent tangent

The equations for the consistent tangent are formed nearly entirely from existing derivatives.

$$\frac{\partial^2 g}{\partial \boldsymbol{\sigma} \partial \boldsymbol{\sigma}} = \Delta\gamma \frac{\partial^2 g}{\partial \sigma_A \partial \sigma_B} \boldsymbol{m}^{(A)} \otimes \boldsymbol{m}^{(B)}, \tag{C.1}$$

$$\frac{\partial^2 g}{\partial \boldsymbol{\sigma} \partial \boldsymbol{q}} = \left[(\partial^2 g / \partial \boldsymbol{\sigma} \partial \boldsymbol{\alpha}) \quad (\partial^2 g / \partial \boldsymbol{\sigma} \partial \kappa) \right] = \left[-(\partial^2 g / \partial \boldsymbol{\sigma} \partial \boldsymbol{\sigma}) \quad (\partial^2 g / \partial \sigma_A \partial \kappa) \boldsymbol{m}^{(A)} \right], \tag{C.2}$$

$$\frac{\partial g}{\partial \boldsymbol{\sigma}} = \frac{\partial g}{\partial \sigma_A} \boldsymbol{m}^{(A)}, \tag{C.3}$$

$$\frac{\partial \boldsymbol{h}^q}{\partial \boldsymbol{\sigma}} = \begin{bmatrix} \partial \boldsymbol{h}^\alpha / \partial \boldsymbol{\sigma} \\ (\partial h^\kappa / \partial \boldsymbol{\sigma})^{\mathrm{t}} \end{bmatrix}, \tag{C.4}$$

$$\frac{\partial \boldsymbol{h}^\alpha}{\partial \boldsymbol{\sigma}} = c^\alpha G^\alpha \mathrm{dev}\left(\frac{\partial^2 g}{\partial \boldsymbol{\sigma} \partial \boldsymbol{\sigma}} \right), \tag{C.5}$$

$$\frac{\partial h^\kappa}{\partial \boldsymbol{\sigma}} = \frac{\partial h^\kappa}{\partial \sigma_A} [\, 1 \quad 1 \quad 1 \quad 0 \quad 0 \quad 0 \,]^{\mathrm{t}}, \tag{C.6}$$

$$\frac{\partial \boldsymbol{h}^q}{\partial \boldsymbol{q}} = \begin{bmatrix} \partial \boldsymbol{h}^\alpha / \partial \boldsymbol{\alpha} & \mathbf{0} \\ \mathbf{0} & \partial h^\kappa / \partial \kappa \end{bmatrix}, \tag{C.7}$$

$$\frac{\partial \boldsymbol{h}^\alpha}{\partial \boldsymbol{\alpha}} = -c^\alpha G^\alpha \mathrm{dev}\left(\frac{\partial^2 g}{\partial \boldsymbol{\sigma} \partial \boldsymbol{\sigma}} \right) + c^\alpha \mathrm{dev}\left(\frac{\partial g}{\partial \boldsymbol{\sigma}} \right) \otimes \frac{\partial G^\alpha}{\partial \boldsymbol{\alpha}}, \tag{C.8}$$

$$\frac{\partial G^{\alpha}}{\partial \boldsymbol{\alpha}} = \frac{-1}{2N\sqrt{J_2^{\alpha}}}\boldsymbol{\alpha}, \tag{C.9}$$

$$\boldsymbol{h}^{q} = \left\{ \begin{array}{c} \boldsymbol{h}^{\alpha} \\ h^{\kappa} \end{array} \right\}, \tag{C.10}$$

$$\boldsymbol{h}^{\alpha} = c^{\alpha} G^{\alpha} \mathrm{dev}\left(\frac{\partial g}{\partial \boldsymbol{\sigma}}\right), \tag{C.11}$$

$$h^{\kappa} = 3\frac{\partial g}{\partial I_1} \Big/ \left(\frac{\partial \epsilon_v^{\mathrm{p}}}{\partial X}\frac{\partial X}{\partial \kappa}\right), \tag{C.12}$$

$$\frac{\partial f}{\partial \boldsymbol{\sigma}} = \frac{\partial f}{\partial \sigma_A}\boldsymbol{m}^{(A)}, \tag{C.13}$$

$$\frac{\partial f}{\partial \boldsymbol{q}} = \left\{ \begin{array}{c} \partial f/\partial \boldsymbol{\alpha} \\ \partial f/\partial \kappa \end{array} \right\}, \tag{C.14}$$

$$\frac{\partial f}{\partial \boldsymbol{\alpha}} = -\frac{\partial f}{\partial \boldsymbol{\sigma}}. \tag{C.15}$$

References

[1] A.A. DiGiovanni, J.T. Fredrich, D.J. Holcomb, W.A. Olsson, Micromechanics of compaction in an analogue reservoir sandstone, in: J. Girard, M. Liebman, C. Breeds, T. Doe (Eds.), Pacific Rocks 2000: Rock Around The Rim, A.A. Balkema, 2000, pp. 1153–1160.

[2] A.F. Fossum, J.T. Fredrich, Cap plasticity models and compactive and dilatant pre-failure deformation, in: J. Girard, M. Liebman, C. Breeds, T. Doe (Eds.), Pacific Rocks 2000: Rock Around The Rim, A.A. Balkema, 2000, pp. 1169–1176.

[3] C. Tamagnini, R. Castellanza, R. Nova, A Generalized Backward Euler algorithm for the numerical integration of an isotropic hardening elastoplastic model for mechanical and chemical degradation of bonded geomaterials, Int. J. Numer. Anal. Methods Geomech. 26 (10) (2002) 963–1004.

[4] R.I. Borja, K.M. Sama, P.F. Sanz, On the numerical integration of three invariant elastoplastic constitutive models, Comput. Methods Appl. Mech. Engrg. 192 (910) (2003) 1227–1258.

[5] J.C. Simo, Algorithms for static and dynamic multiplicative plasticity that preserve the classical return mapping schemes of the infinitesimal theory, Comput. Methods Appl. Mech. Engrg. 99 (1992) 61–112.

[6] J.C. Simo, T.J.R. Hughes, Computational Inelasticity, Prentice-Hall, New York, 1998.

[7] J.C. Simo, Numerical analysis and simulation of plasticity, in: P. Ciarlet, J. Lions (Eds.), Handbook of Numerical Analysis, Elsevier Science, 1998.

[8] I. Doghri, Fully implicit integration and consistent tangent modulus in elastoplasticity, Int. J. Numer. Methods Engrg. 36 (1993) 3915–3932.

[9] S. Hartmann, G. Lührs, P. Haupt, An efficient stress algorithm with applications in viscoplasticity and plasticity, Int. J. Numer. Methods Engrg. 40 (1997) 991–1013.

[10] L.X. Luccioni, J.M. Pestana, R.L. Taylor, Finite element implementation of non-linear elastoplastic constitutive laws using local and global explicit algorithms with automatic error control, Int. J. Numer. Methods Engrg. 50 (2001) 1191–1212.

[11] L. Mähler, M. Ekh, K. Runesson, A class of thermo-hyperelastic viscoplastic models for porous materials: theory and numerics, Int. J. Plast. 17 (2001) 943–969.

[12] M.T. Manzari, R. Prachathananukit, On integration of a cyclic soil plasticity model, Int. J. Numer. Anal. Methods Geomech. 25 (2001) 525–549.

[13] F.J. Montáns, Implicit multilayer J2-plasticity using Prager's translation rule, Int. J. Numer. Methods Engrg. 50 (2001) 347–375.

[14] M. Rouainia, D. Muir Wood, Implicit numerical integration for a kinematic hardening soil plasticity model, Int. J. Numer. Anal. Methods Geomech. 25 (2001) 1305–1325.

[15] J.P.G. Sawyer, C.H. Wang, R. Jones, An implicit algorithm using explicit correctors for the kinematic hardening model with multiple back stresses, Int. J. Numer. Methods Engrg. 50 (2001) 2093–2107.
[16] M. Kobayashi, N. Ohno, Implementation of cyclic plasticity models based on a general form of kinematic hardening, Int. J. Numer. Methods Engrg. 53 (2002) 2217–2238.
[17] A.R. Khoei, A. Bakhshiani, M. Mofid, An implicit algorithm for hypoelasto-plastic and hypoelasto-viscoplastic endochronic theory in finite strain isotropic-kinematic-hardening model, Int. J. Solids Struct. 40 (2003) 3393–3423.
[18] B.D. Coleman, W. Noll, The thermodynamics of elastic materials with heat conduction and viscosity, Arch. Ration. Mech. Anal. 13 (1963) 167–178.
[19] B.D. Coleman, M.E. Gurtin, Thermodynamics with internal state variables, J. Chem. Phys. 47 (1967) 597–613.
[20] A.F. Fossum, R.M. Brannon, The Sandia Geomodel: Theory and User's Guide, SAND report, Sandia National Laboratories, 2004.
[21] P.E. Senseny, A.F. Fossum, T.W. Pfeifle, Non-associative constitutive laws for low porosity rocks, Int. J. Numer. Anal. Methods Geomech. 7 (1983) 101–115.
[22] I.S. Sandler, D. Rubin, An algorithm and a modular subroutine for the CAP model, Int. J. Numer. Anal. Methods Geomech. 3 (2) (1979) 173–186.
[23] I.S. Sandler, F.L. DiMaggio, G.Y. Baldi, Generalized cap model for geological materials, J. Geotech. Engrg. Div. ASCE 103 (12) (1977) 1461.
[24] J.W. Demmel, Applied Numerical Linear Algebra, Society for Industrial and Applied Mathematics, 1997.
[25] T. Belytschko, W.K. Liu, B. Moran, Nonlinear Finite Elements for Continua and Structures, John Wiley & Sons, 2000.
[26] R.W. Ogden, Nonlinear Elastic Deformations, Ellis Horwood, Chicheste, 1984.